Mon. Not. R. Astron. Soc. **317**, 348–374 (2000)

Stellar dynamics in the Galactic Centre: proper motions and anisotropy

R. Genzel,[1★] C. Pichon,[2,3] A. Eckart,[1] O. E. Gerhard[2] and T. Ott[1]

[1]*Max-Planck Institut für Extraterrestrische Physik, D-85740 Garching bei München, Germany*
[2]*Astronomisches Institut, Universität Basel, Switzerland*
[3]*Observatoire de Strasbourg, 11 rue de l'Observatoire, Strasbourg, France*

Accepted 2000 March 20. Received 2000 February 2; in original form 1999 November 8

ABSTRACT

We report a new analysis of the stellar dynamics in the Galactic Centre, based on improved sky and line-of-sight velocities for more than 100 stars in the central few arcseconds from the black hole candidate SgrA*. The main results are as follows.

(1) Overall, the stellar motions do not deviate strongly from isotropy. For those 32 stars with a determination of all three velocity components, the absolute, line-of-sight and sky velocities are in good agreement, consistent with a spherical star cluster. Likewise the sky-projected radial and tangential velocities of all 104 proper motion stars in our sample are also consistent with overall isotropy.

(2) However, the sky-projected velocity components of the young, early-type stars in our sample indicate significant deviations from isotropy, with a strong radial dependence. Most of the bright He I emission-line stars at separations from 1 to 10 arcsec from SgrA* are on tangential orbits. This tangential anisotropy of the He I stars and most of the brighter members of the IRS 16 complex is largely caused by a clockwise (on the sky) and counter-rotating (line of sight, compared to the Galaxy), coherent rotation pattern. The overall rotation of the young star cluster may be a remnant of the original angular momentum pattern in the interstellar cloud from which these stars were formed.

(3) The fainter, fast-moving stars within $\approx$1 arcsec of SgrA* may be largely moving on radial or very elliptical orbits. We have so far not detected deviations from linear motion (i.e., acceleration) for any of them. Most of the SgrA* cluster members are also on clockwise orbits. Spectroscopy indicates that they are early-type stars. We propose that the SgrA* cluster stars are those members of the early-type cluster that happen to have small angular momentum, and thus can plunge to the immediate vicinity of SgrA*.

(4) We derive an anisotropy-independent estimate of the Sun–Galactic Centre distance between 7.8 and 8.2 kpc, with a formal statistical uncertainty of ± 0.9 kpc.

(5) We explicitly include velocity anisotropy in estimating the central mass distribution. We show how Leonard–Merritt and Bahcall–Tremaine mass estimates give systematic offsets in the inferred mass of the central object when applied to finite concentric rings for power-law clusters. Corrected Leonard–Merritt projected mass estimators and Jeans equation modelling confirm previous conclusions (from isotropic models) that a compact central mass concentration (central density $\geq 10^{12.6}\,M_\odot\,pc^{-3}$) is present and dominates the potential between 0.01 and 1 pc. Depending on the modelling method used, the derived central mass ranges between 2.6×10^6 and $3.3\times10^6\,M_\odot$ for $R_\odot = 8.0$ kpc.

Key words: celestial mechanics, stellar dynamics – stars: kinematics – Galaxy: centre – Galaxy: kinematics and dynamics.

1 INTRODUCTION

High spatial resolution observations of the motions of gas and stars have in the past decade substantially strengthened the evidence that central dark mass concentrations reside in many (and perhaps most) nuclei of nearby galaxies (Kormendy & Richstone 1995; Magorrian et al. 1998; Richstone et al. 1998). These dark central masses are very likely to be massive black

★ E-mail: genzel@mpe-garching.mpg.de

holes. The most compelling evidence for this assertion comes from the dynamics of water vapour maser cloudlets in the nucleus of NGC 4258, and from the stellar dynamics in the centre of our own Galaxy (Greenhill et al. 1995; Myoshi et al. 1995; Eckart & Genzel 1996, 1997; Genzel et al. 1997; Ghez et al. 1998). In both cases the gas and stellar dynamics indicate the presence of an unresolved central mass whose density is so large that it cannot be stable for any reasonable length of time unless it is in the form of a massive black hole (Maoz 1998).

The case of the Galactic Centre is particularly intriguing, as it is very close (8 kpc). With the highest spatial resolution observations presently available in the near-infrared ($\leq$0.1 arcsec), spatial scales of a few light-days can be probed. Measurements of both line-of-sight velocities (through Doppler shifts in spectral lines) and sky/proper motions are available and pose very strong constraints on the central mass concentration. The following results have emerged.

(1) The mean stellar velocities (or velocity dispersions) follow a Kepler law ($\langle v^2 \rangle \propto R^{-1}$) from projected radii $R \approx 0.1$ to $\approx$20 arcsec, providing compelling qualitative evidence for the presence of a central point mass (Sellgren et al. 1990; Krabbe et al. 1995; Haller et al. 1996; Eckart & Genzel 1996, 1997; Genzel et al. 1996, 1997; Ghez et al. 1998).

(2) The positions of the dynamical centre (maximum velocity dispersion) and of the maximum stellar surface number density agree with the position of the compact radio source SgrA* (size less than a few au; Lo et al. 1998; Bower & Backer 1998) to within $\pm$0.1 arcsec (Ghez et al. 1998).

(3) Projected mass estimators and Jeans equation modelling of the stellar velocity data indicate that the central mass ranges between 2.2×10^6 and $3 \times 10^6\,M_\odot$. It has a mass-to-luminosity ratio of $M/L > 100\,M_\odot/L_\odot$ and a density $\geq 2 \times 10^{12}\,M_\odot\,pc^{-3}$ (Genzel et al. 1997; Ghez et al. 1998).

The Galactic Centre mass modelling has so far assumed that the stellar velocity ellipsoid is isotropic. An initial comparison of line-of-sight and proper motion velocity dispersions indeed suggests that there are no coarse deviations from isotropy (Eckart & Genzel 1996, 1997). However, to make a more detailed assessment, it is necessary to obtain more accurate stellar motions than were available two years ago. These improved motions – for line-of-sight and sky components – are now in hand and will be analysed in the present paper.

2 OBSERVATIONS AND DATA ANALYSIS

2.1 Proper motions

In our earlier papers (Eckart et al. 1992, 1993, 1994, 1995) we have described the data acquisition and reduction that allowed us to obtain stellar positions with a precision of $\approx$10 milliarcsec per measurement (Eckart & Genzel 1996, 1997; Genzel et al. 1997). We used the MPE-SHARP camera (Hofmann et al. 1993) on the 3.5-m New Technology Telescope (NTT) of the European Southern Observatory (ESO). SHARP contains a 256×256 pixel NICMOS 3 detector. Each pixel projects to 25 or 50 milliarcsec on the sky in order to (over-)sample the $\approx$0.15-arcsec FWHM diffraction-limited image of the NTT in the K band. The raw data for each data set consist of several thousands of short-exposure frames (0.3 to 0.5 s integration time). First, we processed the data from nights with very good seeing (0.4 to 0.8 arcsec) in the standard manner (dead-pixel correction, sky subtraction, flat-fielding etc.). Next, we co-added with the simple-shift-and-add algorithm (SSA) (for details see Christou 1991; Eckart et al. 1994). The individual short-exposure frames typically contain only a few bright speckles, so that the SSA algorithm is well suited for our purpose. The bright infrared sources IRS 7 or IRS 16NE serve as reference sources. For the present study we analysed $\approx$82 independent data sets from a total of nine observing runs in 1992.25, 1992.65, 1993.65, 1994.27, 1995.6, 1996.25, 1996.43, 1997.54 and 1998.37. For the central arcsecond region around SgrA* (the 'SgrA* cluster') we also analysed an additional data set from 1999.42. Eckart & Genzel (1996, 1997) and Genzel et al. (1997) have previously analysed and discussed the data until 1996.43.

The diffraction-limited core of the stellar SSA images contains up to 20 per cent of the light. Determinations of the relative pixel offsets from IRS 16NE in raw SSA images or from diffraction-limited maps after removing the seeing halo give consistent results (see Eckart & Genzel 1996, 1997 for details). These 'CLEANed' SSA maps produce similar results as other data reductions (Knox–Thompson, triple correlation), but give a much higher dynamical range (see Eckart et al. 1994 for a detailed discusssion). This is

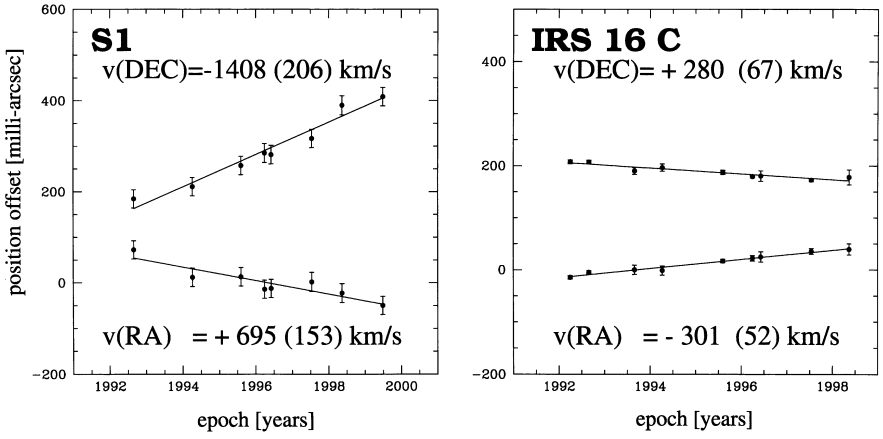

Figure 1. Examples of the proper motions derived from the 1992 to 1998 NTT data sets obtained with the MPE SHARP camera. Shown are position–time plots for source S1 close to SgrA* (left) and the bright He I emission-line star IRS 16C (right). The two panels show x (=RA) and y (=Dec.) position offsets, along with the best-fitting proper motions (straight lines). For each epoch the average and 1σ dispersion of a number position measurements are plotted.

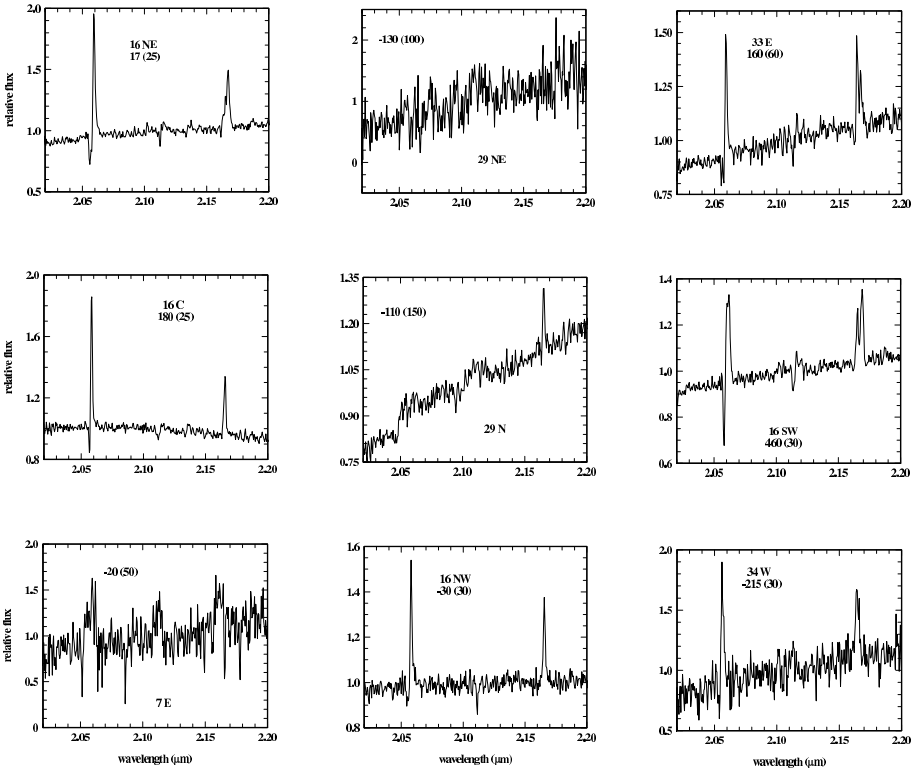

Figure 2. *K*-band spectra of early-type stars in the central ≈10 arcsec obtained in spring 1996 with the MPE 3D spectrometer on the ESO-MPG 2.2-m telescope. The spectral resolving power is $\lambda/\Delta\lambda = 2000$, Nyquist-sampled at twice that resolution. Most of the spectra were obtained by subtracting from the 'on-star' spectrum (0.3 to 1.2 arcsec aperture) and 'off-star' spectrum scaled to the same area, in order to remove local nebular emission. The name is given for each star, as is the stellar velocity in km s^{-1}, with the 1σ uncertainty in parentheses.

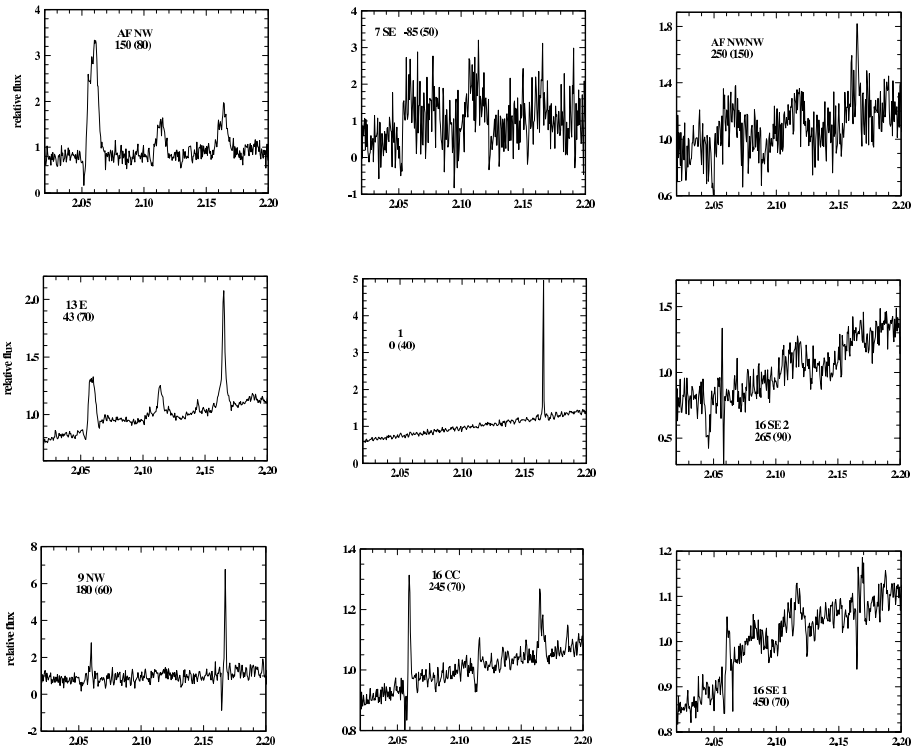

Figure 3. As Fig. 2.

Table 1. Homogenized set of stellar motions in the central parsec.

1 R (SgrA*)	2 Δx (SgrA*) (arcsec)	3 Δy (SgrA*)	4 v_x	5 Δv_x	6 v_y	7 Δv_y	8 v_x	9 Δv_x	10 v_y	11 Δv_y	12 v_{xf}	13 Δv_{xf}	14 v_{yf}	15 Δv_{yf}	16 v_z	17 Δv_z	18 weight	19 name	20 type	21 source	22 K mag	23 variability
									all velocities are in km s^{-1}													
0.11	−0.11	0.04	470	130	−1330	140	695	153	−1408	206	564	99	−1355	116			1	S1	p/early	K/N	14.5	0
0.13	0.11	−0.06	154	259	−79	249					154	259	−79	249			0.25	S3	p/early	NTT	15.1	1
0.15	0.01	0.15	−290	110	−500	100	−101	113	−932	161	−198	79	−621	85			1	S2	p/early	K/N	13.7	0
0.22	0.20	0.09	495	100	300	100	1107	149	62	136	685	83	217	81			1	S4	p/early	K/N	14.3	0
0.33	0.29	0.15	651	155	−187	281					651	155	−187	281			0.25	S5	p/early	NTT	14.6	1
0.34	0.30	−0.15	720	100	−530	110	782	102	−879	187	751	71	−620	95			1	S8	p/early	K/N	14.1	0
0.35	0.21	−0.28	120	140	−630	250	−60	246	−749	456	76	122	−658	219			0.5	S9	p	K/N	14.7	0
0.44	0.15	−0.41	−400	100	230	100	−218	168	−262	250	−352	86	162	93			1	S10	p	K/N	13.8	0
0.45	−0.04	−0.45	138	176	−436	225					138	176	−436	225			0.25	S18	p	NTT	15	
0.46	0.45	0.08	480	170	120	130	104	116	184	105	223	96	159	81			1	S6	p/early	K/N	14.5	0
0.55	0.15	−0.53	200	100	−80	140	624	175	−662	188	304	87	−287	112			1	S11	p	K/N	13.7	0
0.56	−0.12	−0.55	13	265	238	158					13	265	238	158			0.25	S19	p	NTT	15	
0.58	0.30	−0.49	120	100	−50	160	199	260	340	400	130	93	4	149			0.5	–	p	K/N	14.8	
0.60	0.60	−0.02	−130	100	−220	130	−182	100	−461	268	−156	71	−266	117			1	S7	p	K/N	15.1	1
0.63	−0.52	0.35	−100	100	210	100	109	146	88	92	−33	83	144	68			1	W6	p	K/N	14	
0.75	0.59	−0.47	−90	60	250	50					−90	60	250	50			1	–	p	Keck	12.74	0
0.79	−0.74	−0.29	20	90	50	90	35	136	20	79	25	75	33	59			1	W9	p	K/N	13.4	
0.89	0.55	0.70	−450	80	210	80					−450	80	210	80			0.5	–	p	NTT	11.97	1
0.91	−0.85	0.32	−310	60	−310	130	−285	103	−456	73	−304	52	−421	64			1	W5	p	K/N	13.44	
1.01	1.01	0.02	200	90	60	90					200	90	60	90			1	–	p	Keck	12.9	
1.01	−0.91	0.44	−326	70	−518	57					−326	70	−518	57			0.5	–	p	NTT		
1.01	−0.06	−1.01	510	110	90	170					510	110	90	170			0.25	–	p	Keck	13.5	
1.02	0.57	0.84	−480	50	150	70	−581	137	158	90	−492	47	153	55			1	–	p	K/N	11.9	
1.05	0.77	−0.71	410	80	50	100					410	80	50	100			0.5	–	p	Keck	12.34	0
1.05	0.43	−0.96	−300	70	230	80	−218	131	21	85	−282	62	132	58			1	–	p	K/N	12.39	0
1.08	−0.66	−0.85	160	100	−240	70	325	128	−297	53	223	79	−276	42			1	W11	p	K/N	13.8	
1.19	0.03	1.19	310	60	380	110	244	40	35	50	265	33	94	46	−30	30	1	16NW	p/early	all	9.86	0
1.20	−1.20	−0.11	120	170	330	60	−125	200	365	61	17	130	347	43			1	W8	p	K/N	12.52	0
1.29	1.22	0.44	−370	60	380	40	−301	52	280	67	−330	39	353	34	180	25	1	16C	p/early	all	9.55	0
1.32	−0.85	−1.00	220	100	20	100	259	150	−260	120	232	83	−95	77	−1	30	1	W13	pCO	all	13.3	
1.34	−0.84	−1.05	232	115	−287	77					232	115	−287	77			0.5	w217	p	NTT		
1.36	−1.03	−0.88	−410	120	−260	140	−494	130	−410	68	−449	88	−382	61			1	W12	p	K/N	13.8	
1.37	−1.34	−0.29	−20	70	−100	60	−85	120	−272	84	−37	60	−158	49	270	70	1	W10	p/early	all	12.48	0
1.41	−1.31	0.52	30	160	−30	90	−105	118	−193	86	−58	95	−116	62			1	W4	p	K/N	13.9	
1.44	1.06	−0.98	170	60	150	40	360	70	70	70	250	46	130	35	460	30	1	16SW	p/early	all	9.61	2 (double)
1.55	0.55	−1.45	−200	50	−80	50					−200	50	−80	50			1	–	p	Keck	12	
1.63	0.38	−1.58	20	50	−60	120					20	50	−60	120			0.5	–	p	Keck	13.4	
1.64	0.41	1.59	240	80	160	50	299	77	29	53	271	55	98	36			1	–	p	K/N	12.27	0
1.65	−1.65	0.14	160	120	−200	60	−94	126	−185	95	39	120	−196	51			1	W7	p	K/N	13.3	
1.67	−1.65	0.28	−107	114	−127	86					−107	114	−127	86			0.5	–	p	NTT	12.86	0
1.70	−1.63	−0.50	70	60	−5	80	150	135	−83	77	83	55	−45	55			1	W14	p	K/N	12.52	0
1.72	−0.90	−1.46	−20	80	10	90	14	69	−30	50	0	52	−21	44			1	–	p	Keck	11.42	0
1.73	0.76	−1.55	−160	40	−210	70	71	70	−394	41	−103	35	−348	35	−209	30	1	–	pCO	K/N	11.14	0
1.81	1.69	−0.66	−70	90	240	50	132	241	−129	85	−45	84	145	43	−175	30	1	–	pCO	K/N	13.4	
1.89	0.63	−1.78	110	50	−260	50					110	50	−260	50			1	–	p	NTT	11.5	0
2.02	−1.80	0.93	−40	50	50	50	12	112	−2	85	−31	46	37	43	−93	20	1	29S	pCO	all	10.95	0
2.07	−0.54	2.00	140	140	200	40					140	140	200	40			0.5	–	p	Keck	13.8	
2.09	1.46	−1.49	140	70	230	40					140	70	230	40			1	–	p	Keck	11.67	0
2.09	1.91	−0.86	240	110	80	80	36	128	−17	53	154	84	13	44			1	–	p	K/N	12.9	

Table 1 – *continued*

1	2	3	4	5	6	7	8	9	10	11	12	13	14	15	16	17	18	19	20	21	22	23
R (SgrA*)	Δx (SgrA*) (arcsec)	Δy (SgrA*)	v_x	Δv_x	v_y	Δv_y	v_x	Δv_x	v_y	Δv_y	v_{xf}	Δv_{xf}	v_{yf}	Δv_{yf}	v_z	Δv_z	weight	name	type	source	K mag	variability
								all velocities are in km s^{-1}														
2.10	1.60	−1.36	200	60	230	50					200	60	230	50			1	–	p	Keck	11.67	0
2.10	1.06	1.81	−60	90	220	80	−88	64	42	80	−79	52	132	57			1	–	p	K/N	13.2	
2.11	−1.94	0.82	150	110	120	90	0	160	243	117	102	91	166	71			1	W2	p	K/N	11.9	
2.12	2.06	0.51	−120	50	170	60	5	50	250	30	−58	35	234	27	245	70	1	16CC	p/early	all	10.15	0
2.13	−1.59	1.41	200	100	−140	100	174	94	−58	75	186	68	−88	60	−110	150	1	29N	p/early	all	9.74	0
2.13	2.03	−0.63	−130	80	110	70					−130	80	110	70			1	–	p	Keck	11.5	
2.16	−0.02	−2.16	−90	140	−100	90	92	51	−259	30	70	48	−243	28			1	33 N	p/early?	Keck	10.84	0
2.20	1.86	−1.16	170	60	240	40	278	31	50	28	255	28	113	23	450	60	1	16SE1	p/early	all	10.56	0
2.23	−0.91	2.04	−200	90	10	40	−310	50	0	50	−284	44	6	31	−130	100	1	29NE1	p/early	all	11.59	1
2.24	−1.78	−1.36	−342	133	−63	92					−342	133	−63	92			0.25	W15	p	NTT	x	
2.26	1.27	−1.87	260	60	180	40	383	48	−138	40	335	38	21	28			1	–	p/early?	K/N	10.44	0
2.32	−0.90	−2.14	−320	230	140	140	−208	62	−68	40	−216	60	−52	38	102	25	1	–	pCO	all	12.69	0
2.33	0.53	2.27	−180	180	90	40	−258	102	39	43	−239	88	66	29	−107	40	1	–	pCO	all	12.32	0
2.36	−1.70	−1.65	420	110	80	100	−8	124	−58	60	231	82	−22	51			1	–	p	K/N	13.2	
2.39	2.37	−0.29	−140	60	330	40	−42	106	346	234	−116	52	330	39	−143	30	1	–	pCO	all	12.53	0
2.46	−2.28	−0.93	−140	220	110	230	−186	170	166	208	−169	134	141	154			0.25	W16	p	K/N	13.5	
2.59	0.79	−2.46	−200	290	200	200	437	229	−8	100	193	180	33	90			0.25	–	p	K/N	13.7	
2.60	0.73	2.50	340	120	−420	100	442	499	−825	489	346	117	−436	98	−100	30	0.25	–	pCO	all	12.38	0
2.76	0.27	2.74	−170	270	−690	190	−385	82	−21	78	−366	79	−117	72			0.5	–	p	K/N	12.8	0
2.77	−1.80	−2.11	−192	49	34	40					−192	49	34	40			1	–	p	NTT	12.89	0
2.88	−1.14	2.65	−130	50	−140	30					−130	50	−140	30	17	30	1	–	pCO	NTT/LS	11.44	1
2.92	2.91	−0.20	−360	60	140	50	−197	102	28	26	−318	52	52	23			1	–	p	K/N	12.55	0
2.98	1.15	2.75	120	210	260	110	165	65	55	40	161	62	79	38			1	–	p	K/N	11.89	0
3.07	−1.13	2.85	−184	33	−196	57					−184	33	−196	57			0.5	–	p	NTT	x	
3.09	2.89	1.10	160	90	−290	30	242	95	−267	31	199	65	−279	21	17	25	1	16NE	p/early	all	8.76	0
3.12	1.28	2.84	103	48	118	30					103	48	118	30			0.5	–	p	NTT	x	
3.12	3.07	0.56	210	90	80	70	394	209	118	142	239	83	87	63			1	–	p/early?	K/N	11.93	0
3.21	2.97	−1.20	50	90	260	130	192	62	79	61	147	51	111	55	265	90	1	16SE2	p/early	all	11.75	0
3.26	3.26	0.08	90	100	−280	70					90	100	−280	70			0.5	–	p/early?	Keck	12.43	0
3.28	2.01	−2.59	−90	260	200	240	−30	148	−193	124	−44	129	−111	110			0.25	–	p	K/N	13.7	
3.34	0.50	−3.30	211	60	−60	30					211	60	−60	30	160	60	1	33E	p/early	NTT/LS	9.9	0
3.37	−2.85	−1.80													45	60	1	13E	early	LaSilla96	10.26	1
3.45	1.63	−3.04	110	158	−21	48					110	158	−21	48			0.25	–	p	NTT	x	
3.46	−1.80	−2.95	213	60	172	35					213	60	172	35			1	–	p	NTT	11.71	0
3.47	−0.50	−3.43	60	60	30	35					60	60	30	35	82	25	1	33W	pCO	NTT/LS	10.81	0
3.51	3.30	−1.20	−80	70	20	60					−80	70	20	60			0.5	–	p	Keck	11.48	0
3.59	3.40	−1.16	−60	70	−10	120					−60	70	−10	120	−83	25	0.5	–	pCO	K/LS	12.47	0
3.59	3.03	−1.92	−120	200	240	130					−120	200	240	130	47	30	0.25	–	pCO	K/LS	14.4	
3.65	0.79	3.56	113	62	−94	51					113	62	−94	51	−114	40	1	–	pCO	NTT/LS	x	
3.70	2.48	−2.74	−270	170	170	110	−140	70	50	40	−159	65	64	38			1	21	p	K/N	10.61	0
3.80	−3.62	−1.15	8	182	583	149					8	200	583	200	327	60	0.1	–	pCO	NTT/LS	11.73	1
4.08	2.55	3.19	309	159	429	105					309	159	429	105	−85	40	0.1	7SE	p/early	NTT/LS	11.29	0
4.14	3.78	1.70	−160	100	−360	80					−160	100	−360	80			0.5	–	p	Keck	12.35	0
4.32	3.65	−2.32	−100	130	−110	170					−100	130	−110	170			0.25	–	p	Keck	11.22	0
4.39	−4.08	1.62	−80	50	−130	40					−80	50	−130	40	−215	30	1	34W	p/early	NTT/LS	10.86	2
4.44	−2.31	3.79	170	40	115	45					170	40	115	45			1	3	p/early	NTT	10.62	2
4.56	−2.10	−4.05													−55	80	0.25	13SSE	early	LaSilla96	x	
4.67	4.65	0.45													0	30	1	1	early	LaSilla96	8.98	0
4.69	−3.70	2.88	−60	100	−200	80					−60	100	−200	80			0.5	–	p	NTT	12.68	2

Table 1 – *continued*

1 R (SgrA*)	2 Δx (SgrA*) (arcsec)	3 Δy (SgrA*)	4 v_x	5 Δv_x	6 v_y	7 Δv_y	8 v_x	9 Δv_x	10 v_y	11 Δv_y	12 v_{xf}	13 Δv_{xf}	14 v_{yf}	15 Δv_{yf}	16 v_z	17 Δv_z	18 weight	19 name	20 type	21 source	22 K mag	23 variability
									all velocities are in km s^{-1}													
4.81	3.50	−3.30													−15	30	1	–	CO	LaSIII94	12.89	1
4.89	−4.20	−2.50													−74	30	1	13 W	CO	LaSIII94	10.74	2
4.98	−4.60	−1.90													−98	20	1	–	CO	LaSIII94	12.07	1
5.04	5.00	−0.60													−103	25	1	–	CO	LaSIII94	x	
5.16	2.33	4.60	371	156	225	69					371	156	225	69			0.25	–	p	NTT	12.62	0
5.30	5.30	0.10													−178	50	1	–	CO	LaSIII94	10.68	0
5.44	1.90	−5.10													86	25	1	–	CO	LaSIII94	x	
5.57	5.55	0.45													−300	200	0.25	1S	early	LaSilla96	12.63	0
5.58	−1.40	−5.40													17	25	0.5	20	CO	LaSIII94	10.52	0
5.75	0.22	5.75	100	67	−118	35					100	67	−118	35	−103	15	1	7	pCO	NTT/LS	6.37	1
5.77	−0.90	−5.70													32	25	0.5	–	CO	LaSIII94	12.66	1
5.77	−5.70	0.90													−178	40	1	–	CO	LaSIII94	9.49	2
5.79	3.00	−4.95													180	50	1	9NW	early	LaSilla96	12.16	2
5.88	3.10	5.00													72	30	1	–	CO	LaSIII94	12.99	1
5.95	3.90	4.50													−20	50	1	7E	early	LaSilla96	x	
6.04	−5.30	2.90													−68	40	1	–	CO	LaSIII94	x	
6.04	−3.80	−4.70													107	20	1	2S	CO	LaSIII94	10.27	2
6.18	5.70	2.40													−34	30	1	–	CO	LaSIII94	11.85	2
6.35	−3.91	5.00	75	60	−100	80					75	60	−100	80	−300	50	1	7W	p/early	NTT/LS	11.85	2
6.62	6.60	0.50													29	25	1	1NE(3)	CO	LaSIII94	10.86	2
6.72	−6.20	−2.60													−23	20	1	–	CO	LaSIII94	12.41	1
6.77	6.60	1.50													−8	25	1	1NE(2)	CO	LaSIII94	x	
6.86	−4.10	−5.50													117	40	1	–	CO	LaSIII94	11.69	1
7.34	−2.50	6.90													104	40	1	–	CO	LaSIII94		
7.37	7.30	1.00													112	25	1	1NE(1)	CO	LaSIII94	10.37	1
7.47	7.40	−1.00													29	25	1	1SE(1)	CO	LaSIII94	10.73	0
7.52	5.70	−4.90													−79	30	1	–	CO	LaSIII94	x	
7.65	−3.50	−6.80													−96	20	1	12N	CO	LaSIII94	8.86	2
7.80	−6.30	−4.60	20	60	−45	60					20	60	−45	60	−97	30	1	–	pCO	NTT/LSS	11.66	2
7.83	7.00	3.50													7	30	1	10EW	CO	LaSIII94	x	
7.94	−0.86	7.89	−194	90	13	48					−194	90	13	48			1	26	p	NTT	11.06	0
7.96	−3.80	7.00													−153	80	0.5	–	CO	LaSIII94		
8.03	−7.10	3.75	−70	80	−120	80					−70	80	−120	80			0.5	–	p	NTT	12.06	2
8.04	−5.70	5.67	60	60	75	30					60	60	75	30	−77	30	1	BHA4E	pCO	NTT/LS	10.55	1
8.10	3.50	7.30													−6	50	1	–	CO	LaSIII94	11.51	1
8.26	−8.10	1.60													−150	70	1	6W	early	LaSilla94	10.9	2
8.33	−2.56	7.93	189	85	−52	59					189	85	−52	59			0.5	86	p	NTT	12.83	1
8.34	−7.20	−4.20													150	70	1	AFNW	early	LaSilla96	x	
8.42	−1.90	8.20													−33	30	1	–	CO	LaSIII94	x	
8.49	2.20	−8.20													88	25	1	–	CO	LaSIII94	12.19	1
8.59	5.50	6.60													77	40	1	–	CO	LaSIII94	x	
8.61	8.40	1.90													108	30	1	–	CO	LaSIII94	12.5	2
8.82	0.60	−8.80													19	20	1	14N	CO	LaSIII94	9.45	1
8.82	−6.45	6.02	−270	100	175	100					−270	100	175	100	100	30	0.25	BHA4W	pCO	NTT/LS	10.44	2
8.99	6.00	−6.70													−283	25	1	–	CO	LaSIII94	x	
9.04	0.90	9.00													23	30	1	–	CO	LaSIII94	x	
9.06	5.50	−7.20													−300	25	1	9	CO	LaSIII94	8.94	2
9.09	8.30	3.70													−55	30	1	10EE	CO	LaSIII94	11.56	2
9.45	7.30	−6.00													−58	35	1	–	CO	LaSIII94	x	

Table 1 – *continued*

1 R (SgrA*)	2 Δx (SgrA*) (arcsec)	3 Δy (SgrA*)	4 v_x	5 Δv_x	6 v_y	7 Δv_y	8 v_x	9 Δv_x	10 v_y	11 Δv_y	12 v_{xf}	13 Δv_{xf}	14 v_{yf}	15 Δv_{yf}	16 v_z	17 Δv_z	18 weight	19 name	20 type	21 source	22 K mag	23 variability
									all velocities are in km s^{-1}													
9.53	−0.70	−9.50													29	20	1	14SW	CO	LaSIII94	10.98	0
9.55	−9.10	2.90													−135	40	1	–	CO	LaSIII94	x	
9.69	−3.60	−9.00													51	25	0.5	12S	CO	LaSIII94	9.94	2
9.73	−9.15	−3.30													250	100	1	AFNWW	early	LaSilla96	11.67	2
9.86	−9.80	−1.10													−50	30	1	–	CO	LaSIII94	x	
9.90	9.30	−3.40													22	50	1	–	CO	LaSIII94	x	
9.91	−7.30	−6.70													140	50	1	AF	early	LaSilla94	10.51	2
10.01	3.70	9.30													67	40	1	–	CO	LaSIII94	x	
10.03	−8.25	−5.70													170	70	0.5	–	early	LaSilla96	11.9	1
10.06	6.70	−7.50													−283	30	1	–	CO	LaSIII94	x	
10.08	5.10	8.70													147	30	1	–	CO	LaSIII94	x	
10.21	−1.50	10.10													−230	50	1	15SW	early	LaSilla94	x	
10.33	2.60	−10.00													19	30	0.5	–	CO	LaSIII94	x	
10.44	−3.60	9.80													134	25	1	–	CO	LaSIII94	x	
10.47	−9.20	−5.00													−20	70	1	Blum	early	LaSilla94	x	
10.51	9.40	−4.70													82	40	1	–	CO	LaSIII94	x	
10.60	8.30	−6.60													−103	35	1	–	CO	LaSIII94	12.77	1
10.61	10.60	0.50													227	25	1	–	CO	LaSIII94	x	
10.72	5.50	−9.20													200	50	1	9S	early	LaSilla94		
11.18	7.60	8.20													105	35	1	–	CO	LaSIII94		
11.24	11.20	−1.00													177	30	1	–	CO	LaSIII94		
11.30	−5.80	9.70													7	30	1	–	CO	LaSIII94		
11.32	−8.20	7.80													77	30	1	–	CO	LaSIII94		
11.38	−8.10	−8.00													−18	30	1	–	CO	LaSIII94		
11.41	−10.10	−5.30													87	50	1	–	CO	LaSIII94		
11.47	1.30	11.40													17	25	1	15N	CO	LaSIII94		
11.50	−8.80	7.40													59	30	1	–	CO	LaSIII94		
11.51	1.60	11.40													−80	50	1	15NE	early	LaSilla94	11.4	2
11.52	−2.70	11.20													−68	30	1	–	CO	LaSIII94	x	
11.61	−11.00	−3.70													−8	40	1	–	CO	LaSIII94	x	
11.74	9.50	6.90													12	50	1	–	CO	LaSIII94	12.62	2
11.83	−0.90	11.80													45	20	1	–	CO	LaSIII94		
11.87	6.70	9.80													37	30	1	–	CO	LaSIII94	x	
11.91	4.80	10.90													121	30	1	–	CO	LaSIII94	x	
11.98	−4.50	11.10													−88	50	1	–	CO	LaSIII94	x	
12.00	0.20	−12.00													41	30	1	–	CO	LaSIII94	x	
12.01	11.90	−1.60													107	30	1	–	CO	LaSIII94	x	
12.02	11.50	3.50													137	25	1	–	CO	LaSIII94	x	
12.05	3.60	11.50													57	30	1	–	CO	LaSIII94	x	
12.25	11.80	−3.30													27	60	1	–	CO	LaSIII94	x	
12.48	5.50	−11.20													171	35	1	–	CO	LaSIII94	x	
12.59	10.60	−6.80													–93	25	1	28	CO	LaSIII94	x	
12.66	−9.20	8.70													42	50	1	–	CO	LaSIII94	x	
12.71	11.60	5.20													114	25	1	–	CO	LaSIII94	x	
12.76	3.40	−12.30													112	20	1	BHA17	CO	LaSIII94	x	
12.95	12.50	−3.40													347	60	1	–	CO	LaSIII94	x	
13.06	−6.20	11.50													−23	50	1	–	CO	LaSIII94	x	
13.11	6.10	11.60													111	30	1	–	CO	LaSIII94	x	
13.15	7.50	−10.80													18	40	1	–	CO	LaSIII94		

Table 1 – *continued*

1 R (SgrA*)	2 Δx (SgrA*) (arcsec)	3 Δy (SgrA*)	4 v_x	5 Δv_x	6 v_y	7 Δv_y	8 v_x	9 Δv_x	10 v_y	11 Δv_y	12 v_{xf}	13 Δv_{xf}	14 v_{yf}	15 Δv_{yf}	16 v_z	17 Δv_z	18 weight	19 name	20 type	21 source	22 K mag	23 variability
								all velocities are in km s^{-1}														
13.22	13.20	−0.70													187	30	1	–	CO	LaSIII94		
13.28	8.50	10.20													97	30	1	–	CO	LaSIII94		
13.30	9.10	−9.70													−138	70	1	–	CO	LaSIII94		
13.34	11.70	6.40													67	40	1	–	CO	LaSIII94		
13.49	13.20	2.80													106	40	0.5	–	CO	LaSIII94		
13.50	−0.20	−13.50													−38	50	1	–	CO	LaSIII94		
13.66	−1.30	13.60													−45	50	1	–	CO	LaSIII94		
13.67	10.20	9.10													−56	40	1	–	CO	LaSIII94		
13.87	5.10	−12.90													137	40	1	–	CO	LaSIII94		
13.88	−13.10	−4.60													−93	50	1	–	CO	LaSIII94		
13.90	11.50	−7.80													−163	30	1	–	CO	LaSIII94		
13.98	12.90	−5.40													−36	50	1	–	CO	LaSIII94		
14.04	6.40	−12.50													87	35	1	–	CO	LaSIII94		
14.06	13.10	5.10													185	25	1	17	CO	LaSIII94		
14.06	−7.80	−11.70													−73	40	1	–	CO	LaSIII94		
14.06	−11.70	7.80													130	60	1	–	CO	LaSIII94		
14.25	14.20	−1.20													−183	50	1	–	CO	LaSIII94		
14.37	−5.90	−13.10													−58	70	1	–	CO	LaSIII94		
14.38	−11.60	−8.50													72	25	1	–	CO	LaSIII94		
14.48	3.70	14.00													117	60	1	–	CO	LaSIII94		
14.58	−10.80	9.80													77	45	1	–	CO	LaSIII94		
14.64	−8.80	−11.70													−45	40	1	BHA2	CO	LaSIII94		
14.64	5.90	13.40													−83	70	1	–	CO	LaSIII94		
14.65	10.70	10.00													67	40	1	–	CO	LaSIII94		
14.71	−14.00	4.50													33	50	1	–	CO	LaSIII94		
14.88	−5.80	13.70													−48	40	1	–	CO	LaSIII94		
15.03	2.00	−14.90													64	25	1	–	CO	LaSIII94		
15.08	6.30	−13.70													31	50	1	–	CO	LaSIII94		
15.11	13.00	−7.70													−38	40	1	–	CO	LaSIII94		
15.19	11.60	−9.80													34	35	1	–	CO	LaSIII94		
15.21	−3.50	−14.80													67	60	1	–	CO	LaSIII94		
15.25	−13.80	6.50													32	50	1	–	CO	LaSIII94		
15.31	15.30	0.40													−73	70	1	–	CO	LaSIII94		
15.35	−7.30	13.50													27	40	1	–	CO	LaSIII94		
15.37	−4.50	−14.70													−33	70	1	–	CO	LaSIII94		
15.59	−9.70	12.20													−24	30	1	11SW	CO	LaSIII94		
15.78	14.90	5.20													121	30	1	–	CO	LaSIII94		
15.81	−13.20	8.70													3	35	1	–	CO	LaSIII94		
15.86	−10.60	−11.80													−63	40	1	–	CO	LaSIII94		
16.01	−0.60	−16.00													19	40	1	–	CO	LaSIII94		
16.04	2.10	15.90													57	50	1	–	CO	LaSIII94		
16.10	6.10	14.90													92	50	1	–	CO	LaSIII94		
16.18	2.40	−16.00													−28	60	1	–	CO	LaSIII94		
16.18	12.80	−9.90													50	40	1	–	CO	LaSIII94		
16.20	11.80	−11.10													81	35	1	–	CO	LaSIII94		
16.30	4.40	15.70													−36	60	1	–	CO	LaSIII94		
16.35	−8.60	13.90													14	30	1	11NE	CO	LaSIII94		
16.35	4.20	−15.80													−151	80	1	–	CO	LaSIII94		
16.46	−16.40	1.40													−60	60	0.5	–	CO	LaSIII94		

Table 1 – *continued*

1 R (SgrA*)	2 Δx (SgrA*) (arcsec)	3 Δy (SgrA*)	4 v_x	5 Δv_x	6 v_y	7 Δv_y	8 v_x	9 Δv_x	10 v_y	11 Δv_y	12 v_{xf}	13 Δv_{xf}	14 v_{yf}	15 Δv_{yf}	16 v_z	17 Δv_z	18 weight	19 name	20 type	21 source	22 K mag	23 variability
									all velocities are in km s^{-1}													
16.46	14.50	−7.80													50	60	1	–	CO	LaSIII94		
16.49	10.40	−12.80													−138	50	1	–	CO	LaSIII94		
16.65	−16.00	4.60													−129	50	1	–	CO	LaSIII94		
16.77	−13.00	−10.60													−103	40	1	–	CO	LaSIII94		
16.95	−3.90	−16.50													−148	50	1	–	CO	LaSIII94		
16.98	−9.00	−14.40													37	40	1	–	CO	LaSIII94		
17.01	−16.90	1.90													97	40	1	–	CO	LaSIII94		
17.42	−6.40	16.20													−118	70	1	–	CO	LaSIII94		
17.45	1.30	−17.40													70	50	1	–	CO	LaSIII94		
17.49	−15.50	8.10													163	25	1	–	CO	LaSIII94		
17.54	8.40	−15.40													27	60	0.5	–	CO	LaSIII94		
17.66	−1.50	17.60													107	30	1	–	CO	LaSIII94		
17.98	−6.40	−16.80													−213	60	1	–	CO	LaSIII94		
18.02	−8.10	16.10													−29	50	0.5	–	CO	LaSIII94		
18.08	−7.40	−16.50													−84	50	0.5	–	CO	LaSIII94		
18.10	0.20	−18.10													17	30	1	–	CO	LaSIII94		
18.15	−9.60	−15.40													−63	40	1	–	CO	LaSIII94		
18.20	−9.20	15.70													−8	50	0.5	–	CO	LaSIII94		
18.28	11.00	−14.60													17	70	0.5	–	CO	LaSIII94		
18.28	9.70	−15.50													107	70	0.5	–	CO	LaSIII94		
18.30	0.20	−18.30													0	30	1	–	CO	LaSIII94		
18.34	−5.80	17.40													−8	60	1	–	CO	LaSIII94		
18.51	0.50	18.50													−53	60	1	–	CO	LaSIII94		
18.54	−3.00	−18.30													−203	50	1	BHA7	CO	LaSIII94		
18.58	15.60	−10.10													2	40	1	–	CO	LaSIII94		
18.66	−17.00	7.70													87	40	1	–	CO	LaSIII94		
18.81	13.40	−13.20													7	50	1	–	CO	LaSIII94		
18.92	17.50	−7.20													−93	60	1	–	CO	LaSIII94		
19.01	−5.50	−18.20													−63	80	1	–	CO	LaSIII94		
19.03	−10.60	−15.80													157	70	1	–	CO	LaSIII94		
19.36	15.50	−11.60													27	35	1	18	CO	LaSIII94		
19.49	12.80	−14.70													122	40	1	–	CO	LaSIII94		
19.60	14.40	−13.30													77	50	1	–	CO	LaSIII94		
19.91	17.10	−10.20													77	50	1	–	CO	LaSIII94		
19.92	−6.60	−18.80													−20	40	1	–	CO	LaSIII94		
20.00	18.50	−7.60													72	60	1	–	CO	LaSIII94		
20.04	3.10	−19.80													−158	60	1	–	CO	LaSIII94		
20.17	17.90	−9.30													−3	60	1	–	CO	LaSIII94		
20.30	−4.90	−19.70													−85	40	1	–	CO	LaSIII94		
20.37	−2.60	20.20													−53	60	1	–	CO	LaSIII94		
20.68	16.70	−12.20													−123	50	1	–	CO	LaSIII94		
20.73	−8.30	−19.00													87	100	0.2	–	CO	LaSIII94		
20.73	−1.20	−20.70													−23	30	1	–	CO	LaSIII94		
20.79	14.80	−14.60													−23	50	1	–	CO	LaSIII94		
20.90	18.30	−10.10													7	70	0.5	–	CO	LaSIII94		
21.16	19.20	−8.90													−23	60	1	–	CO	LaSIII94		
21.21	3.00	−21.00													−60	60	1	–	CO	LaSIII94		
21.52	−4.70	−21.00													35	60	1	–	CO	LaSIII94		
21.80	18.20	−12.00													207	100	0.2	–	CO	LaSIII94		

Table 1 – *continued*

1	2	3	4	5	6	7	8	9	10	11	12	13	14	15	16	17	18	19	20	21	22	23
R (SgrA*)	Δx (SgrA*) (arcsec)	Δy (SgrA*)	v_x	Δv_x	v_y	Δv_y	v_x	Δv_x	v_y	Δv_y	v_{xf}	Δv_{xf}	v_{yf}	Δv_{yf}	v_z	Δv_z	weight	name	type	source	K mag	variability
										all velocities are in km s^{-1}												
21.92	15.20	−15.80													−73	50	1	–	CO	LaSII94		
22.00	16.80	−14.20													−113	60	1	–	CO	LaSII94		
22.05	19.60	−10.10													−68	40	1	–	CO	LaSII94		
22.13	1.20	−22.10													−3	30	1	–	CO	LaSII94		
22.60	0.40	−22.60													72	60	1	–	CO	LaSII94		

essential in the crowded Galactic Centre region where the difference between the brightest and faintest stars in our images is almost 10 mag. We solved for the relative offsets, rotation angle, and for the linear and quadratic distortions between individual frames from an over-determined system of non-linear equations for a reference list of relatively isolated bright stars (Eckart & Genzel 1996, 1997). Our final near-infrared reference frame is tied to an accuracy of ±30 milliarcsec to the VLA radio frame through five stars that show SiO and H_2O maser activity and are common to both wavelength bands (Menten et al. 1997). The resulting combined systematic errors in our proper motion velocity estimates are probably about 30 km s^{-1}. In the best cases these systematic effects now dominate the error budget.

The new 1997 and 1998 data sets are in excellent agreement with the extrapolation of the data we have published before, and significantly improve the uncertainties. As examples we show in Fig. 1 the relative RA and Dec. position offsets as a function of time between 1992 and 1998 for two selected stars. IRS 16C is a bright and isolated, He I emission-line star (Krabbe et al. 1991, 1995). Its position versus time diagram in Fig. 1 is an example of the quality of the data on bright isolated stars. S1 is a faint star in the 'SgrA* cluster' that is very close to SgrA* (≈0.1 arcsec). It shows the fastest proper motion (≈1470 km s^{-1}) in the entire sample.

2.2 3D spectroscopy

We observed the Galactic Centre with the MPE-3D near-infrared spectrometer (Weitzel et al. 1996) in conjunction with the tip-tilt adaptive optics module ROGUE (Thatte et al. 1995). 3D is a field-imaging spectrometer which obtains spectra simultaneously for 256 spatial pixels covering a square region of the sky (16 × 16 pixels). The fill factor is over 95 per cent. For further details of the instrument and data reduction we refer to Weitzel et al. We observed the Galactic Centre in 1996 March at the 2.2-m ESO-MPG telescope on La Silla, Chile. During the run the seeing on the seeing monitor ranged between 0.3 and 0.8 arcsec. The pixel scale was 0.3 arcsec. We observed the short-wavelength part of the K band (1.9–2.2 μm) at $\lambda/\Delta\lambda = 2000$, Nyquist-sampled with two settings of a piezo-driven flat mirror. We covered the central ≈16 × 10 arcsec^2 centred on SgrA* by an overlapping set of frames, each with a field of view of 4.8 × 4.8 arcsec^2. At each position we set up a sequence on-source (piezo step 1), off-source (piezo step 1), on-source (piezo step 2), off-source (piezo step 2), etc., with an integration time per step of 200 s. Due to the combined effects of seeing and pixel scale the resulting FWHM spatial resolution of the final combined data set was 0.6 arcsec. We employed the standard 3D data analysis package (based on GIPSY; van der Hulst et al. 1992). We performed wavelength calibration, sky subtraction, spectral and spatial flat-fielding, dead- and hot-pixel correction, and division by a reference stellar spectrum obtained during the observations. We corrected for the effects of a spatially varying fringing or 'channel' spectrum due to interference in the saphire coating of the NICMOS 3 detector by applying suitable flat-fields from a set of flat-fields at different settings of the piezo mirror. Based on observations of calibration lamps and OH sky lines during the different observing nights, the final velocity calibration is accurate to ±16 km s^{-1}.

In the observed field we identified 21 emission-line stars from continuum-subtracted images of the 2.058-μm $n = 2\ ^1\mathrm{P} - n = 2\ ^1\mathrm{S}$ and 2.11-μm $n = 4\ ^{3,1}\mathrm{S} - n = 3\ ^{3,1}\mathrm{P}$ He I lines, and the

2.166-μm $n = 7$–4 H I (Brγ) line. Most of the stars are identical with those found in the ≈1-arcsec, $R = 1000$ 3D data set of Krabbe et al. (1995) and Genzel et al. (1996) (see also Haller et al. 1986, Blum, Sellgren & dePoy 1995a and Blum, dePoy & Sellgren 1995b), but the resolution, quality and nebular rejection is now much superior. Three new stars were identified: (−2.″1, −4.″1) (13S SE), (+1.″6, +0.″3) (16CC) and (−8.″3, −5.″7) (all offsets are in RA and Dec. from SgrA*). We extracted from the data cube spectra of individual stars by typically averaging 3 to 16 pixels on the star, for effective apertures between 0.3 and 1.2 arcsec. In most cases we subtracted a suitable 'off-star' spectrum (scaled to the same aperture area) to eliminate the effect of local nebular line emission. Figs 2 and 3 show the final spectra for 18 of the 21 stars.

To determine stellar velocities, we fitted Gaussians to the 2.058- and 2.11-μm He I lines, and the 2.166-μm Brγ line. In a few cases we also used the 2.137/2.143-μm Mg II lines and the 2.189-μm He II line. A number of the stars clearly display P Cygni profiles in the 2.058-μm He I transition (Figs 2 and 3). In these cases we fitted the profile with a double Gaussian (absorption and emission). As the absorption structure is well resolved, an unambiguous emission-line centroid (assumed to be the stellar velocity) can thus be easily obtained. For most stars we determined the final stellar velocities from averaging the values obtained from 3 (or 4) lines. The agreement between the fits to the different lines is generally good and sometimes excellent. We list the final velocities in Table 1 and the insets of Figs 2 and 3. The new velocity determinations agree with those of Genzel et al. (1996), but the uncertainties are typically half of those in our earlier work. The best cases have an uncertainty of $\pm 25\,\mathrm{km\,s^{-1}}$.

2.3 A homogenized data set

To obtain a homogenized 'best' data set of stellar velocities for further analysis, we combined the new 1992–1998 NTT proper motions and 2.2-m line-of-sight velocity data described in the last two paragraphs with the 1995–1997 Keck proper motion data of Ghez et al. (1998) and with other relevant line-of-sight velocity data sets (see Genzel et al. 1996, and references therein). Table 1 gives the results. The following explanations and comments for Table 1 are in order.

(1) Columns 1 to 3 contain the projected separation R, the x(= RA) offset and the y(= Dec.) offset between star and SgrA* (epoch 1994/1995, all in arcseconds). As for the NTT, the Keck astrometry is established with H_2O/SiO maser stars that are visible in both wavelength bands, and is accurate to ±10 milliarcsec (see Menten et al. 1997 and Ghez et al. 1998).

(2) Columns 4 to 11 contain the x and y proper motions and their respective 1σ errors ($\mathrm{km\,s^{-1}}$, for a Sun–Galactic Centre distance of $R_\odot = 8.0$ kpc). Whenever two measurements are available, we first list the velocity from the Keck observations, and then that from the NTT observations. Columns 12 to 15 give the final combined proper motions obtained from averaging motions from the two sets (if available) with $1/\sigma^2$ weighting. The agreement between Keck and NTT data sets is generally very good (see discussion by Ghez et al. 1998), and is in accordance with the measurement uncertainties. We thus assume that the final measurement error of the combined set is given by $1/\sqrt{(1/\sigma_1^2 + 1/\sigma_2^2)}$. We have found, however, from a comparison of the two data sets that stars with $>200\,\mathrm{km\,s^{-1}}$ velocity uncertainty at $R \geq 1$ arcsec (and $>400\,\mathrm{km\,s^{-1}}$ at $R \leq 1$ arcsec) are highly unreliable. We have therefore eliminated such stars from the final set.

(3) Columns 16 and 17 give the line-of-sight-velocity and its 1σ error.

(4) Column 18 assigns a weight to each data point, based on its reliability, the velocity errors and the agreement between different data sets. The weight is approximately proportional to 1/error^2, as appropriate for white noise, but 'quantized' in order not to place too much weight on the few data points with the smallest statistical errors. While this weighting scheme is subjective, it is in our opinion a fair representation of the quality of the different data points in the presence of significant systematic errors. We have also tried another, more formal weighting scheme. Here we have assigned the weight $w = 1/[1 + (\mathrm{error}/\sigma_0)^2]$, where 'error' is the x/y-averaged proper motion velocity uncertainty. $\sigma_0 = 250R^{-0.5}$ is a measure of the sample dispersion at R. This weighting scheme also gives essentially the same weights for different data points, as long as their individual errors are much smaller than the sample velocity dispersion. For large errors the weight scales as 1/error^2 as for white noise. We have applied both weighting schemes in the various estimates discussed in the text. The results are basically identical.

(5) Column 19 lists the 'popular' name of the star.

(6) Column 20 lists an identification; 'p' stands for a star with a measured proper motion, 'early' denotes that the star is a young early-type star (e.g., He I/H I emission lines), and 'CO' denotes that the star is a late-type star.

(7) Column 21 lists the source(s) of measurement for the specific data point [Keck (K) and NTT (N) for proper motions, LaSilla (LS), or 'all'].

(8) Column 22 lists the K magnitude of the star, and column 23 makes a statement on its variability. If available, we used the K magnitudes from the comprehensive variability study of Ott et al. (1999); otherwise we list the magnitudes of Ghez et al. (1998), corrected for $\delta m_K = -0.4$ to account for a small calibration offset between the Ott et al. and Ghez et al. sets. If the value in the last column is 0, the star was not, or not significantly, variable in the 1992 to 1998 monitoring campaign of Ott et al. A value of 1 indicates that the star showed a statistically significant but weak variability. A value of 2 indicates that the star was strongly variable in the Ott et al. observations.

3 KINEMATICS OF THE GALACTIC CENTRE STAR CLUSTER

The velocity determinations in Table 1 are significantly improved over our earlier work and over Ghez et al. (1998). Many light-of-sight and sky velocities now have errors less than $50\,\mathrm{km\,s^{-1}}$, with the best velocity determinations (± 20 to $25\,\mathrm{km\,s^{-1}}$) mainly limited by systematic effects (e.g., establishing reference frame from the moving stars themselves and removing distortions in the imaging), rather than by statistical errors (positional accuracy of stellar positions). Of the 2×104 proper motions in Table 1, 48 (23 per cent) are determined to 4σ or better. Five proper motions are determined at the $\geq 10\sigma$ level. Of the 227 line-of-sight velocities, 38 (17 per cent) are determined to 4σ or better. For 14 (of 29) He I emission-line stars and for 18 late-type stars we now have determinations of all three velocity components. With this improved data set it is now possible to investigate in more detail the kinematic parameters of individual stars and/or small groups of stars. In order to remove as far as possible measurement and

calibration bias and zero-point offsets, we subtract in all of our calculations below for each velocity measurement i the mean velocity of the sample $\langle v\rangle$ linearly and the velocity uncertainty error (v_i) in squares when computing velocity dispersions, etc.,

$$(v_i^2)_{\rm intrinsic} = [(v_i - \langle v\rangle)^2]_{\rm measured} - error^2(v_i). \quad (1)$$

3.1 Tests for anisotropy

As proposed by Eckart & Genzel (1996, 1997), a first simple (but coarse) test for anisotropy in the data (and/or a Sun–Galactic Centre distance significantly different from $R_\odot = 8$ kpc) is to compare the sky and line-of-sight velocities of individual stars. Fig. 4 is a plot of $\gamma_{pz} = (v_{prop}^2 - v_z^2)/(v_{prop}^2 + v_z^2)$ as a function of projected separation R for the 32 stars with three measured velocities. Here v_{prop} is the root mean square of the x and y sky motions, and v_z is the line-of-sight motion. In this plot, stars with $\gamma_{pz} = -1$ have $v_z \gg v_{prop}$, and stars with $\gamma_{pz} = +1$ have $v_z < v_{prop}$. Fig. 4 shows no obvious sign for such an anisotropy. This is probably not surprising as the line-of-sight and sky velocities both contain linear combinations of the intrinsic radial and tangential components of the velocity ellipsoid. The result in Fig. 4 that the sample expectation value for the proper motion velocity dispersion is the same (within statistical uncertainties) as the line-of-sight dispersion, $\langle v_{prop}^2\rangle \simeq \langle v_z^2\rangle$, is consistent with the assumption that we are observing a spherically symmetric cluster. The virial theorem guarantees that this results holds, independent of internal anisotropy (see equations 7, 8 and 9).

To investigate intrinsic kinematic anisotropies, it is therefore necessary to explicitly decompose the observed motions into projections of the intrinsic velocity components. Assuming that the velocity ellipsoid of a selected (sub) sample of stars separates in spherical coordinates and denoting the components of velocity dispersion parallel and perpendicular/tangential to the radius vector r as σ_r and σ_t, the line-of-sight component $\hat\sigma_z(R,z)$ is then given by

$$\hat\sigma_z^2 = \sigma_r^2(r)\cos^2\theta + \sigma_t^2(r)\sin^2\theta, \quad (2)$$

where $\cos\theta = \boldsymbol{r}\cdot\boldsymbol{z}/r$, and $\boldsymbol{z}$ is the unit vector along the line of sight. The components of the velocity dispersion parallel (R) and perpendicular (T) to the projected radius vector on the sky R are given by

$$\hat\sigma_R^2 = \sigma_r^2(r)\sin^2\theta + \sigma_t^2(r)\cos^2\theta, \quad (3)$$

and

$$\hat\sigma_T^2 = \sigma_t^2(r). \quad (4)$$

Given the spatial density distribution $n(r)$ of the selected sample of stars (assumed to be spherically symmetric), the line-of-sight-averaged, density-weighted value of the projected radial velocity dispersion of the sample at R, σ_R, can then be computed from the relationship

$$\Sigma(R)\sigma_R^2(R) = \int_{-\infty}^{\infty} n(z)(\sigma_r^2(r)\sin^2\theta + \sigma_t^2(r)\cos^2\theta)\,{\rm d}z$$
$$= 2\int_R^{\infty}[\sigma_r^2(r)(R/r)^2 + \sigma_t^2(r)(1-(R/r)^2]\frac{n(r)r\,{\rm d}r}{(r^2-R^2)^{1/2}}, \quad (5)$$

where $\Sigma(R)$ is the stellar surface density at R,

$$\Sigma(R) = 2\int_R^{\infty}\frac{n(r)r\,{\rm d}r}{(r^2-R^2)^{1/2}}. \quad (6)$$

Similar equations hold for $\sigma_T^2(R)$ and $\sigma_z^2(R)$. The global expectation value of the projected radial dispersion is given by

$$\langle\sigma_R^2\rangle = (2\pi/N)\int_0^{\infty}\int_0^{\pi} n(r)r^2[\sigma_r^2(r)\sin^2\theta + \sigma_t^2(r)\cos^2\theta]\sin\theta\,{\rm d}\theta\,{\rm d}r$$
$$= 2/3\langle\sigma_r^2\rangle + 1/3\langle\sigma_t^2\rangle, \quad (7)$$

where N is the number of stars in the selected sample. Likewise one finds

$$\langle\sigma_z^2\rangle = (2\pi/N)\int_0^{\infty}\int_0^{\pi} n(r)r^2[\sigma_r^2(r)\cos^2\theta + \sigma_t^2(r)\sin^2\theta]\sin\theta\,{\rm d}\theta\,{\rm d}r$$
$$= 1/3\langle\sigma_r^2\rangle + 2/3\langle\sigma_t^2\rangle, \quad (8)$$

and

$$\langle\sigma_T^2\rangle = \langle\sigma_t^2\rangle \quad (9)$$

(Leonard & Merritt 1989). Deviations of the velocity ellipsoid from isotropy are commonly expressed in terms of the anisotropy parameter $\beta = 1 - \sigma_t^2/\sigma_r^2$. Its globally averaged value is given by

$$\langle\beta\rangle = 1 - \langle\sigma_t^2\rangle/\langle\sigma_r^2\rangle = 3(\langle\sigma_R^2\rangle - \langle\sigma_T^2\rangle)/(3\langle\sigma_R^2\rangle - \langle\sigma_T^2\rangle). \quad (10)$$

An isotropic cluster ($\langle\beta\rangle = 0$) has $\langle\sigma_r\rangle = \langle\sigma_t\rangle$ and $\langle\sigma_R\rangle = \langle\sigma_T\rangle$. A cluster with only radial orbits ($\langle\beta\rangle = 1$) has $\langle\sigma_t\rangle = \langle\sigma_T\rangle = 0$ or $\langle\sigma_R\rangle \gg \langle\sigma_T\rangle$. A cluster with only tangential orbits ($\langle\beta\rangle = -\infty$) has $\langle\sigma_r\rangle = 0$ and $\langle\sigma_R\rangle = \langle\sigma_T\rangle/\sqrt{3}$. Thus radial anisotropy is easier to see in the proper motions than tangential anisotropy. Table 2 gives the values of $\langle\sigma_R\rangle$, $\langle\sigma_T\rangle$, $\langle\sigma_R\rangle/\langle\sigma_T\rangle$ and $\langle\beta\rangle$, computed for all stars with proper motions and for different ranges of projected radii from SgrA*. Errors in these quantities are derived from statistics and error propagation. Below we use Monte Carlo simulations to investigate the uncertainties in the derived anisotropy parameters more thoroughly. The proper motions of the entire sample of stars, as well as the stars in the range $R \geq 3$ arcsec, are consistent with isotropy. At $R = 1$ to 3 arcsec there is a (marginal) trend for the stars to be more on tangential orbits. In the central arcsecond the stars on average appear to be on radial orbits. The statistical significance of this departure from isotropy for the 17 stars at $R \leq 0.8$ arcsec from SgrA* appears to be 3.3σ in terms of

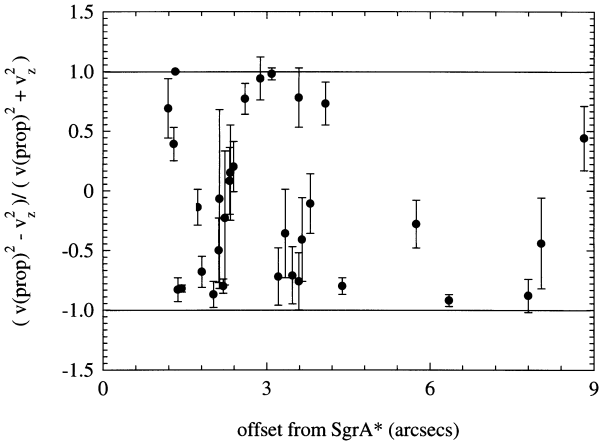

Figure 4. The anisotropy parameter $\gamma_{pz} = (v_{prop}^2 - v_z^2)/(v_{prop}^2 + v_z^2)$ for all 32 stars with all three velocity components measured. Error bars are determined through error propagation from the velocity uncertainties in Table 1.

Table 2. Velocity dispersions, anisotropies and projected mass estimators.

Annulus	N (stars)	$\langle R \rangle$ (arcsec)	σ_T (km s^{-1})	σ_R (km s^{-1})	σ_T/σ_R	β	M(BT)	M(VT) (10^6 M$_\odot$)	M(LM)
$0 < R < 0.8''$	17	0.3	334(58)	503(88)	0.66(0.15)	0.66(0.2)			
$0 < R < 1''$	19	0.4	347(57)	479(79)	0.72(0.14)	0.58(0.23)	2.2(0.5)	2.2(0.7)	2.4(0.8)
$1 < R < 2''$	26	1.4	243(34)	168(24)	1.45(0.29)	−3.6(6.1)	2.8(0.5)	2.7(0.8)	2.5(0.7)
$2 < R < 3''$	26	2.3	175(25)	135(19)	1.30(0.26)	−1.54(2.3)	3.2(0.6)	2.8(0.8)	2.8(0.8)
$3 < R < 5''$	23	3.5	153(22)	148(22)	1.03(0.21)	−0.11(0.72)	3.6(0.7)	3.0(0.9)	3.6(1.1)
$5 < R < 9''$	9	7.3	115(28)	117(28)	0.98(0.34)	0.06(0.9)	3.7(1.2)	3.8(1.8)	3.6(1.7)
$0 < R < 5''$	95	1.4	236(17)	250(18)	0.94(0.1)	0.15(0.23)	3.06(0.31)	2.62(0.38)	2.91(0.42)
			243(18)	246(18)	0.99(0.1)	0.04(0.29)	3.14(0.32)	2.46(0.36)	2.93(0.42)

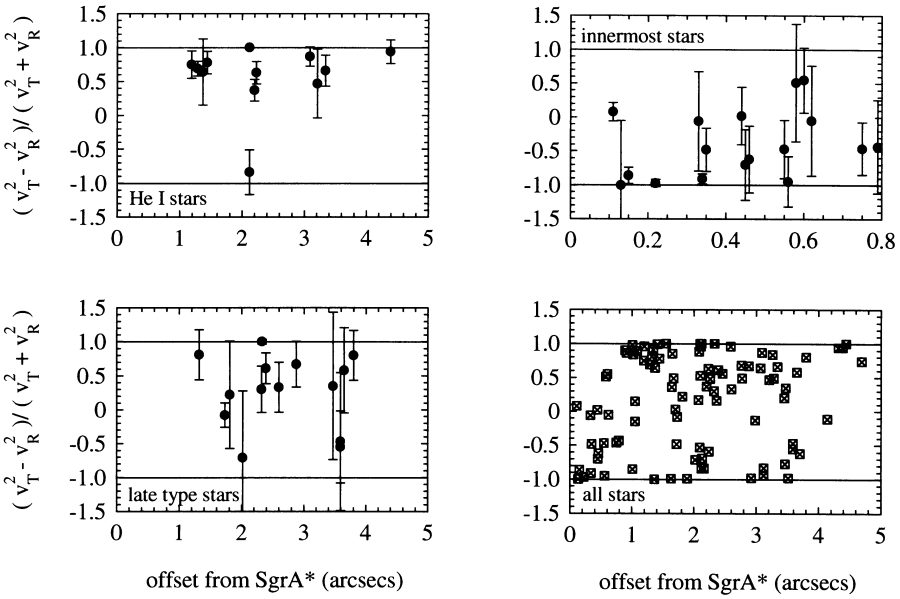

Figure 5. The anisotropy parameter $\gamma_{TR} = (v_T^2 - v_R^2)/(v_T^2 + v_R^2)$ for the 12 He I stars within $R \leq 5$ arcsec (top left), for the 14 late-type stars within $R \leq 5$ arcsec (bottom left), for all stars inside 5 arcsec with proper motions (bottom right), and for stars within $R \leq 0.8$ arcsec of SgrA* (top right). Error bars are determined through error propagation from the velocity uncertainties in Table 1.

propagated errors for β (Table 2); however, the Monte Carlo simulations in Section 4.3 below show that the distribution of β is very broad, and the isotropic $\beta = 0$ is still within somewhat more than 1σ equivalent for such a small sample. Excluding the faint stars in the SgrA* cluster at $R \leq 1$ arcsec, the remaining proper motions between $R = 1$ and 5 arcsec deviate from isotropy in the direction of tangential orbits at the 2σ level.

A second and more sensitive test for anisotropy is a comparison of the projected radial (v_R) and projected tangential (v_T) components of the sky velocities of individual stars. Fig. 5 gives plots of $\gamma_{TR} = (v_T^2 - v_R^2)/(v_T^2 + v_R^2)$ for different selections of our data. Considering all 104 proper motions, Fig. 5 (bottom right) indicates a fairly even distribution of γ_{TR}s, without obvious overall bias indicating anisotropy, perhaps a slight predominance of tangential orbits (compare Fig. 9). The same is true if only the late-type stars of the proper motion sample are considered (Fig. 5, bottom left).

A different and fairly clear-cut picture emerges when one considers the (much younger) early-type stars. Fig. 5 (top left) clearly indicates that with one exception all bright He I emission-line stars within $R = 5$ arcsec are on projected tangential orbits ($\gamma_{TR} \approx +1$) and therefore (see the discussion after equation 10) largely on true tangential or circular orbits. In contrast, more than half of the faint ($m_K \approx 13$ to 16) stars within 1 arcsec of SgrA* (SgrA* cluster) are predominantly on radial ($\gamma_{TR} \leq 0$) orbits (top right panel of Fig. 5). *We conclude that the early-type stars in our proper motion set do show significant anisotropy.* We will show below that the main cause of the tangential anisotropy is a global rotation of the early-type stars.

3.2 Orbits for the innermost stars

We have also modelled the orbits of several of the individual fast-moving stars in the SgrA* cluster. As an example, we plot in Fig. 6 the measured 1992–1999 NTT positions of S1 and S2 with respect to SgrA*, along with the projection of a few possible trajectories. The three plotted orbits represent extreme choices of the orbital parameters in the potential of a central compact mass. For orbit A we assumed the largest possible current separation from SgrA* for bound orbits with $v_z = 0$. For orbit B we took the largest line-of-sight-velocity at $z = 0$ under the boundary condition that S1 and S2 are still bound to SgrA*. The assumption that S1/S2 are in the same plane of the sky as the central mass and have no line-of-sight-velocity results in the orbit with the largest curvature (orbit C). Although no unique orbit can yet be determined from the data,

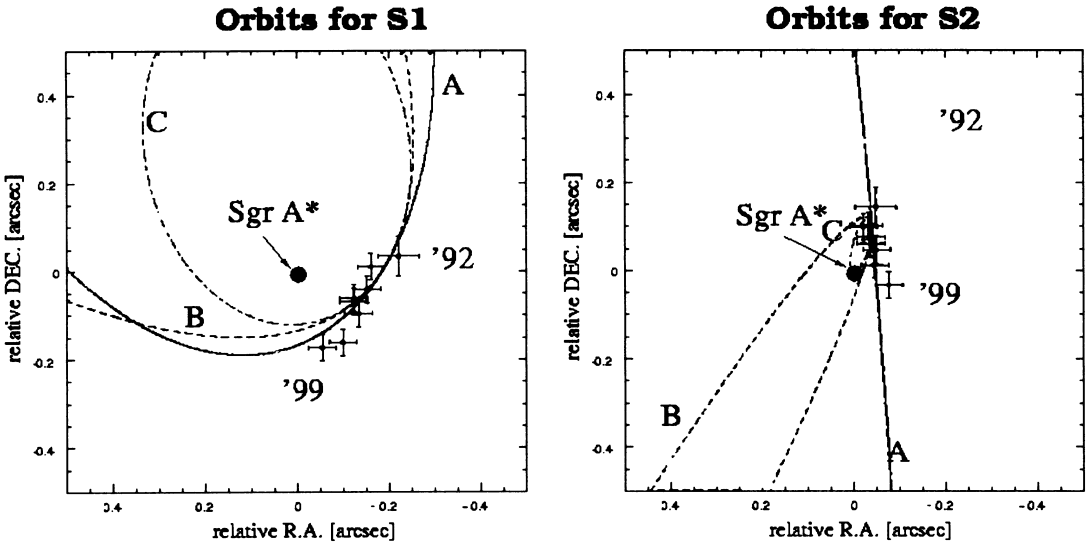

Figure 6. Possible orbits for S1 and S2, the stars closest to SgrA*. The positions of S1(left) and S2 (right) between 1992 and 1999, and their uncertainties, are shown as crosses. Three possible bound orbits in the potential of a 2 to $3 \times 10^6\,M_\odot$ point mass are shown. Orbit A (continuous curve) has the largest possible separation from SgrA*, and orbit B (short dashes) the largest line-of-sight-velocity. The assumption that S1 and S2 are in the same plane of the sky as the central mass and have no line-of-sight-velocity results in the orbit with the largest curvature (orbit C, dot-dashed).

our analysis shows that most of the high-velocity stars in the SgrA* cluster can be bound to a central mass of $3 \times 10^6\,M_\odot$ with a distribution of line-of-sight positions and velocities that is consistent with the projected dimensions and velocity dispersion of the cluster. *Orbits with radii of curvature comparable to their projected radii from SgrA* (orbit C) can already be excluded for these stars*. S1, S2 and several other fast-moving stars around SgrA* must be on plunging (radial) orbits or on very elliptical/parabolic orbits with semi-axes much greater than the current projected separations from SgrA*, as already indicated by the analysis of the velocities in the preceding paragraph. The stellar orbits in the central cluster will not be simple closed ellipses. Especially for orbits with large eccentricities, node-rotation due to the non-Keplerian potential in the extended stellar cluster, as well as relativistic periastron rotations, will make the trajectories for the individual stars 'rosette'-like. A more detailed analysis of orbits has to await longer time baselines for the proper motion measurements and the detection of orbit curvature (=acceleration), as well as measurements of the line-of-sight-velocities of the central stars.

3.3 Anisotropy and relaxation time

These deviations from isotropy for the early-type stars are consistent with their young ages as compared to the relaxation time. Within the central stellar core, the two-body relaxation time for a star of mass m_{10} (in units of $10\,M_\odot$) is given by

$$t_r(m) = 10^{7.58}\sigma_{100}^3/[\rho_{6.6} m_{10}(\ln N_*/13)] \quad \text{(yr)}. \tag{11}$$

Here $\rho_{6.6}$ is the density of the nuclear star cluster (in units of $4 \times 10^6\,M_\odot\,pc^{-3}$), and σ_{100} is the velocity dispersion in units of $100\,km\,s^{-1}$ within the core radius[1] of 0.38 $(+0.25, -0.15)$ pc (Genzel et al. 1996). N_* is the number of stars in the core (≈ 3–5×10^5). The lifetime of the upper main sequence phase scales approximately as $t_{ms} \approx 10^{7.2} m_{10}^{-1.9}$ yr, and the duration of the red-/blue-giant or supergiant phases is typically 10 to 30 per cent of t_{ms} (e.g. Meynet et al. 1994). The ratio of relaxation time to stellar lifetime is thus

$$\chi = t_r/t_{ms} \approx 2.4 m_{10}^{0.9}. \tag{12}$$

A number of authors have shown have shown that the He I emission-line stars are high-mass (30 to $120\,M_\odot$), post-main-sequence blue supergiants (Allen, Hyland & Hillier 1990; Krabbe et al. 1991, 1995; Najarro et al. 1994, 1997; Blum et al. 1995a,b; Libonate et al. 1995; Tamblyn et al. 1996; Ott et al. 1999). Their ages range between $t \approx 2$ and 9×10^6 yr (Najarro et al. 1994, 1997; Krabbe et al. 1995). The massive stars are probably the 'tip of the iceberg' of a component of young stars of total mass $\approx 10^4\,M_\odot$ that were formed a few million years ago in an extended starburst episode (Krabbe et al. 1995). The massive stars are somewhat older than their main-sequence age. Their main-sequence lifetime is much greater than the dynamical time-scale ($t_{ms} \gg t_{dyn} \simeq 10^3$ yr), but they have not had time to dynamically relax through multiple interactions with other stars ($\chi \gg 1$). Their present kinematic properties thus reflect the initial conditions with which they were born, and the starburst must have been triggered near their present orbits. The situation is different for the observed late-type stars. For M giants of mass 1.5 to $3\,M_\odot$ (and ages $\geq 10^9$ yr) and for luminous asymptotic giant branch (AGB) stars of mass 3 to $8\,M_\odot$ (and ages $\geq 10^8$ yr), χ is comparable to or smaller than unity. Such stars should have had sufficient time to be scattered and relax in the central potential.

4 MONTE CARLO SIMULATIONS

Because the velocity measurement errors are often large and the number of measured velocities is still relatively small, we need to investigate the expected errors in the velocity anisotropy in more detail to get a more quantitative estimate whether the observed anisotropy is statistically significant. Therefore we now describe theoretical 'measurements' on Monte Carlo star clusters with

[1] The core radius is defined here as the radius where the stellar density has fallen to half its central value.

comparable numbers of stars. The next subsection describes the models from which the artificial data are drawn.

4.1 Anisotropic distribution functions

We construct some simple anisotropic, scale-free spherical distribution functions $f(\varepsilon,h)$ for stars with specific energy ε and specific angular momentum h in a potential ψ. These are computed from the formula (for a derivation and its generalization to non-integer index n, see, e.g., Pichon & Gerhard, in preparation):

$$f(\varepsilon,h) = (-\varepsilon)^{n+\frac{1}{2}} \frac{\sqrt{2}}{4\pi\sqrt{\pi}\,\Gamma\left(\frac{3}{2}+n\right)} \left(\frac{\mathrm{d}}{\mathrm{d}\,r^2\psi}\right)^{n+2} r^{2n+4}\rho(r)\Bigg|_{r^2\psi\to h^2/2}, \tag{13}$$

where the specific energy and angular momentum are given by

$$\varepsilon = \tfrac{1}{2}(v_r^2+v_t^2) - \psi \quad \text{and} \quad h = rv_t. \tag{14}$$

Neglecting the self-gravity of the star cluster in the vicinity of the central black hole, we write

$$\psi(r) = \frac{GM}{r}, \quad \text{and} \quad \rho(r) = \rho_0\left(\frac{r}{r_0}\right)^{-5/2}, \tag{15}$$

where M is the black hole mass, and G the gravitational constant. The slope of the cluster density profile is chosen to provide a compromise between the observed $m(K) \leq 15$ number counts (see below) and the observed distribution of the innermost SgrA* cluster stars.

The resulting distribution from equations (13)–(15) reads

$$f(\varepsilon,h) \propto (-\varepsilon)^{n+\frac{1}{2}} h^{2n-1} = \frac{3\sqrt{-\varepsilon}}{64\,h\pi^3}, \frac{35(-\varepsilon)^{\frac{3}{2}}\,h}{128\pi^3}, \frac{231(-\varepsilon)^{\frac{5}{2}}\,h^3}{256\pi^3},$$

$$\frac{1287(-\varepsilon)^{\frac{7}{2}}\,h^5}{512\,\pi^3}, \frac{46189(-\varepsilon)^{\frac{9}{2}}\,h^7}{7168\pi^3}, \frac{96577(-\varepsilon)^{\frac{11}{2}}\,h^9}{6144\pi^3} \tag{16}$$

$$\propto (-\varepsilon)[h/h_c(\varepsilon)]^{2n-1} \tag{17}$$

for $n = 0, 1, \cdots 5$. Here $h_c(\varepsilon)$ denotes the angular momentum of the circular orbit at energy ε. The units are such that the total mass and scale-radius, r_0, of the star cluster are unity and $GM = 1$. For this simple scale-free cluster in a Keplerian potential the distribution functions are also derived in sections 2.2 and 3.1 of Gerhard (1991).

The velocity dispersion corresponding to equation (13) is

$$\frac{\partial}{\partial r^2\psi}(\sigma_r^2\rho r^{2n+6}) = r^{2n+4}\rho, \tag{18}$$

and together with the Jeans equation

$$\frac{\mathrm{d}}{\mathrm{d}r}(\rho\sigma_r^2) + \frac{2\beta}{r}\rho\sigma_r^2 = -\frac{\rho\,GM}{r^2}, \tag{19}$$

this implies

$$\beta_* = 1/2 - n, \tag{20}$$

where the $*$ subscript refers to the fact that this is the *intrinsic* anisotropy of the model. These simple models are therefore scale-free and have constant anisotropy parameters β_*, which in the following will be chosen to match the range of values found for the Galactic Centre data set.

4.2 Monte Carlo star clusters

We generate N stars sampled regularly in radius with a cumulative mass profile corresponding to equation (15). These are also required to obey equation (16), i.e., the number of stars at radius r within $\mathrm{d}r$ with radial velocity v_r within $\mathrm{d}v_r$ and tangential velocity v_t within $\mathrm{d}v_t$ is given by

$$\mathrm{d}N = 8\pi^2 r^2 v_t f\left(\tfrac{1}{2}\left(v_r^2+v_t^2\right) - \psi(r), rv_t\right) \mathrm{d}r\,\mathrm{d}v_t\,\mathrm{d}v_r. \tag{21}$$

Given a triplet (r,v_r,v_t), we generate a random position vector $\boldsymbol{r} = r\{\cos(\theta)\cos(\phi), \cos(\theta)\sin(\phi), \sin(\theta)\}$ where z is along the line of sight as before, ϕ is a random number uniform in the range $[0,2\pi]$ and $\sin(\theta)$ is a random number uniform in $[-1,1]$. We also construct $v_\theta = v_t\cos(\chi)$ and $v_\phi = v_t\sin(\chi)$, where χ is a random number uniform in $[0, 2\pi]$. The velocity vector then reads $\boldsymbol{v} = v_r\boldsymbol{e_r} + v_\theta\boldsymbol{e_\theta} + v_\phi\boldsymbol{e_\phi}$. It is then straightforward to project the components of $\boldsymbol{r}$ and $\boldsymbol{v}$ on to the plane of the sky.

Fig. 7 displays sky projections of the proper motion vectors of 250 stars drawn from $\beta_* = 1/2$ and $-1/2$ clusters, respectively. The length of each arrow is proportional to the magnitude of the projected proper motion. The figure shows that a radially anisotropic cluster is readily recognized by the many stars with radial proper motions: intrinsically radial orbits remain radial when projected on to the sky, and the number of radial proper motions is a good indicator of the number of radial orbits. By contrast, intrinsically tangential orbits may appear tangential or radial in the sky plane, depending on the orientation of their orbital planes. Correspondingly, the projection of the tangentially anisotropic cluster in Fig. 7, while showing fewer radial and more tangential proper motion vectors, still contains a significant number of the former. Therefore, tangentially anisotropic clusters are more difficult to recognize and discriminate from each other in terms of their apparent proper motion distributions. Once the model is sufficiently tangential, the ratio of radial to tangential proper motions is largely determined by the projection rather than by the intrinsic anisotropy.

4.3 Anisotropy estimators

From the Monte Carlo sample of stars we can estimate the previously used anisotropy indicators γ_{TR}, and $\langle\beta\rangle$ (equation 10). The histograms of the estimated γ_{TR} in Fig. 8 confirm the above discussion quantitatively. (i) They show that radially anisotropic models are more easily recognized by their proper motion anisotropy than tangentially anisotropic models. None the less, strongly tangentially anisotropic clusters are recognizable in terms of their many stars with γ_{TR} near $+1$. (ii) The distribution of γ_{TR} is slightly skewed towards positive values even for near-isotropic clusters. (iii) The histograms are always bimodal, i.e., they have peaks near $\gamma_{TR} = \pm 1$. This is also recognizable in the data; cf. the bottom right panel of Fig. 5.

These histograms are discrete realizations of the probability distribution for γ_{TR}, and this in turn derives from the marginal probability distribution for the intrinsic quantity $\gamma_{tr} = (v_t^2 - v_r^2)/(v_r^2+v_t^2)$, i.e., the number of stars with γ_{tr} in a small interval $\mathrm{d}\gamma_{tr}$. Once the distribution function is known, this is straightforward to compute:

$$\mathrm{pdf}(\gamma_{tr})\,\mathrm{d}\gamma_{tr} \propto \left[\int f(\varepsilon(v_r[v_t,\gamma_{tr}],v_t), rv_t)\frac{\partial v_r}{\partial\gamma_{tr}} v_t\,\mathrm{d}v_t\right]\mathrm{d}\gamma_{tr},$$

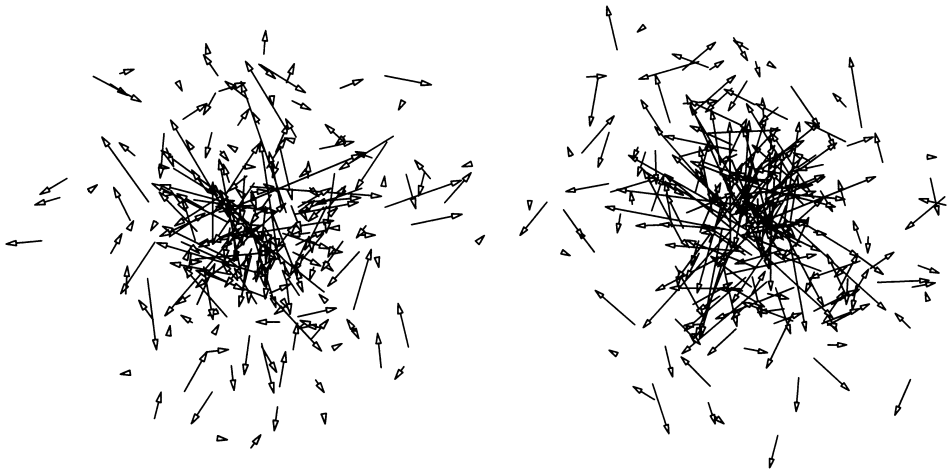

Figure 7. *Left-hand panel:* Sky projection of 250 proper motions drawn from a star cluster with $\rho \propto r^{-2.5}$ and $\beta_* = 1/2$ (radial anisotropy) and *right-hand panel:* $\beta_* = -1/2$ (tangential anisotropy) in the potential of a point mass. The distinction between radially and tangentially anisotropic clusters is clearly visible. Radially anisotropic clusters are more easily recognizable on the basis of the proper motion patterns than tangentially anisotropic clusters. Note that it may appear incorrectly that most stars are moving outwards, because the inner plunging orbits have longer vectors and seem to be moving radially outwards as the arrows overshoot the centre.

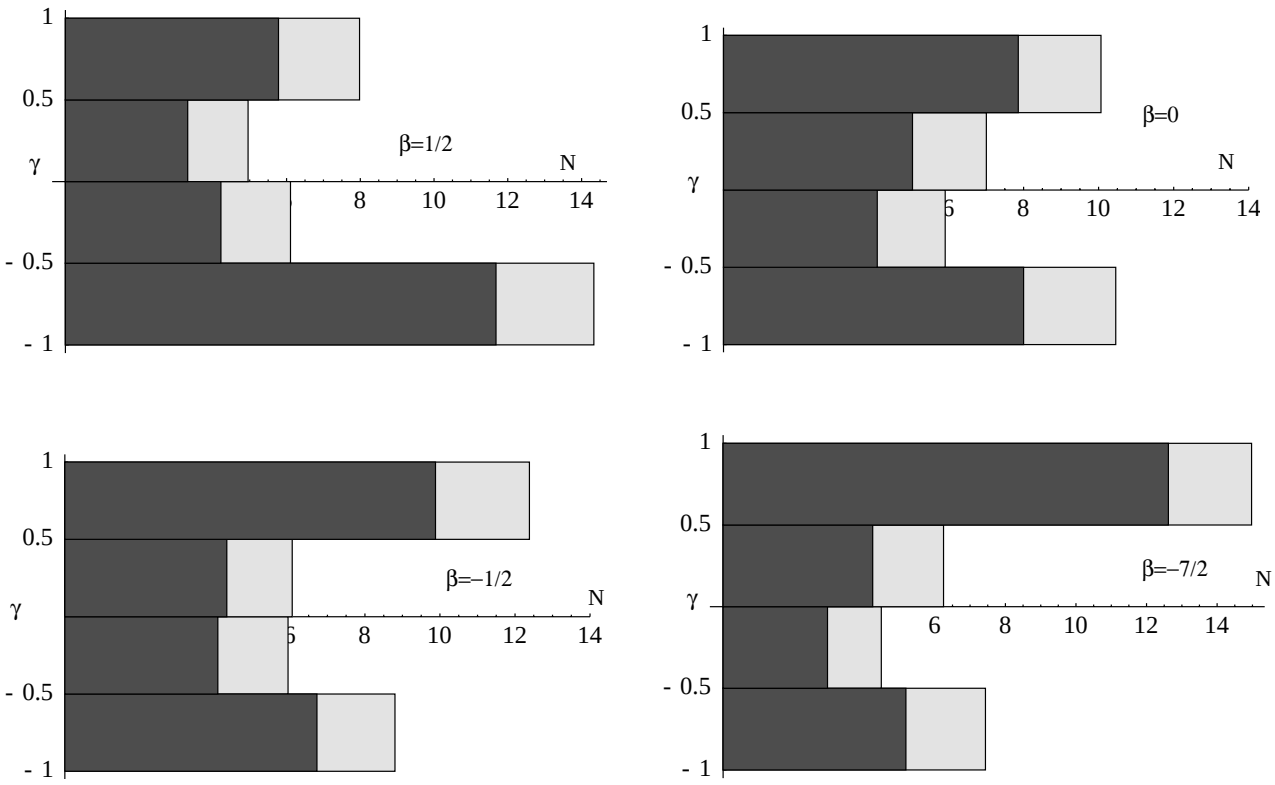

Figure 8. Histograms of $\gamma_{TR} = (v_T^2 - v_R^2)/(v_T^2 + v_R^2)$ for a total number of 25 stars drawn from the simulations described in Section 4. Dark histograms show the mean number of stars per bin averaged over 50 draws of 25 stars each out of a 5000 stars cluster. The added light histogram shows the mean relative errors of the bin values. From top to bottom and left to right: $\beta_* = 0.5, 0, -0.5, -3.5$. Note that the isotropic model shows more stars on projected tangential orbits than on projected radial orbits.

which yields (after normalization)

$$\mathrm{pdf}(\gamma_{tr})\,\mathrm{d}\gamma_{tr} = \frac{n!(\sqrt{1+\gamma_{tr}})^{2n-1}}{\pi(2n-1)!!\sqrt{1-\gamma_{tr}}}\mathrm{d}\gamma_{tr},$$

$$\text{where} \quad (n)!! = n(n-2)(n-4)\cdots 1. \tag{22}$$

This pdf is illustrated in Fig. 9; it is strongly non-Gaussian and skewed for both $n > 0$ and for an isotropic cluster. The reason why the isotropic curve is not symmetric is because we have defined γ_{tr} in terms of the total v_t^2 on the sphere rather than one-half that. The main point of this diagram is the non-uniform and sometimes bimodal shape of the distribution. The distribution of the *observed* γ_{TR} pdf after projection is also shown in Fig. 9 as a histogram for

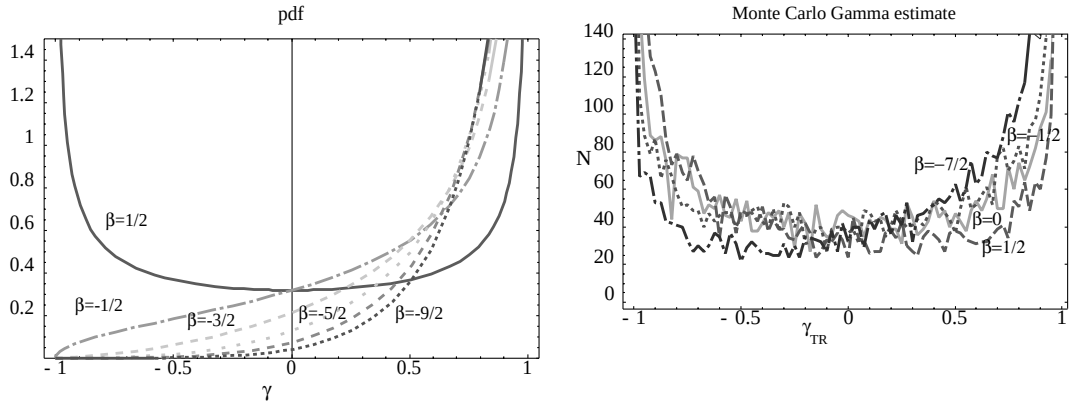

Figure 9. *Left-hand panel:* Theoretical γ_{tr} probability distribution (pdf) for star clusters with constant anisotropy given by $\beta_* = 1/2, -1/2, -3/2, -5/2, -7/2, -9/2$, corresponding to expectation values for γ_{tr} of $n/(n+1) = 0$, 1/2, 2/3, 3/4, 4/5 and 5/6 and variances of $(1+2n)/(1+n)^2\,/(2+n) = 1/2$, 1/4, 5/36, 7/80, 3/50 and 11/252. These distributions are very non-Gaussian and are peaked near ± 1. The $\beta_* = 1/2$ curve is symmetric (unlike the isotropic model), because we have defined γ_{tr} in terms of the total v_t^2 on the sphere rather than one-half that. For these pdfs the mean and standard deviation are well–defined for all values of $\beta*$. *Right-hand panel:* Projected γ_{TR} pdf for 2000 stars in clusters with $\beta_* = 1/2$, 0, $-1/2$, $-7/2$ (dashed, full, dotted, and long dash-dotted lines). As for γ_{tr}, none of these curves is uniform. Note that all pdfs have significant tails for $\gamma_{TR} = -1$, because even purely tangential orbit may project to projected radial orbits on the sky. Most of the difference between the various models is in the relative number of stars in the radial and tangential peaks near ± 1. The most tangentially anisotropic model (long dash-dotted line) has the most stars for $\gamma_{TR} \in [0.5, 1]$, whereas the radially anisotropic cluster (dashed line) is overabundant in near-radial proper motions. The curve for the isotropic cluster is nearly symmetric.

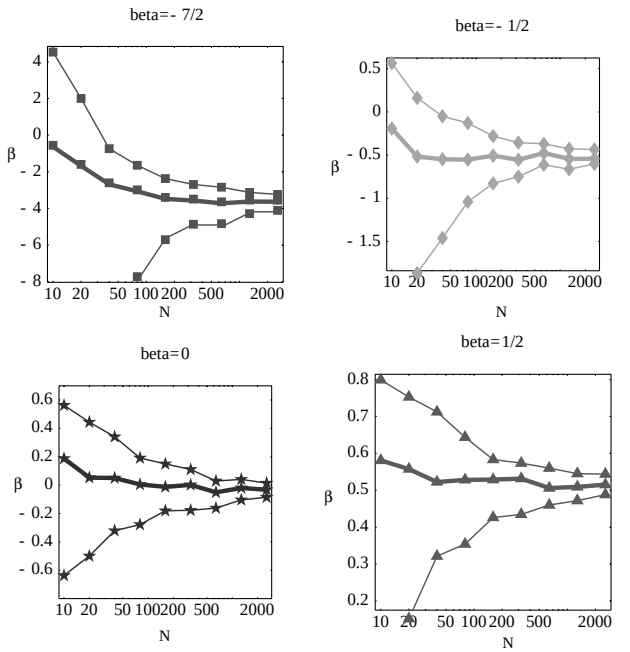

Figure 10. Median (thick line) and first and third quartiles (thin lines) for the distribution of $\langle\beta\rangle$ values determined by equation (10), from simulated proper motion samples, as a function of sample size (per bin) and for several values of true $\beta*$ for the underlying star cluster. The asymmetric width of the confidence bands reflects the asymmetric nature of the anisotropy parameter β. For small samples equation (10) allows unphysical derived values for β. Note the drift of the median as a function of N, which also reflects the fact that the pdf of $\hat{\beta}$ has inherited that of β, with both being skewed towards negative values; see equation (23) and Fig. 11. The rather slow convergence of the estimator as a function of the number of stars for models with more negative β is striking; this follows indirectly from equation (23), which has no well-defined moments.

5000 stars. Relative to the intrinsic pdf the number of (projected) radial orbits has been boosted, as discussed above; the distribution is now always bimodal. Thus in diagrams like Fig. 6 we should always expect to find an overabundance of stars near $\gamma_{TR} = \pm 1$ compared to values near $\gamma_{TR} \simeq 0$, with the ratio $N(\gamma_{TR} \lesssim 1)/N(\gamma_{TR} \gtrsim -1)$ containing the information about anisotropy.

Fig. 10 shows the median and first and third quartiles for the distribution of $\langle\beta\rangle$ values determined by equation (10) from simulated proper motion samples, as a function of sample size and for several values of true $\beta*$ for the underlying star cluster. These confidence bands are especially wide for negative values of $\beta*$, because it is a very asymmetric indicator of anisotropy. Indeed, the marginal probability distribution for the β values as determined from *individual* stellar velocities is given by (following the derivation of equation 22)

$$\frac{pdf(\beta)\,\mathrm{d}\beta = \sqrt{2}2^{2n}n!(\sqrt{1-\beta})^{2n-1}}{\pi(2n-1)!!(3-2\beta)^{n+1}\mathrm{d}\beta.} \tag{23}$$

This pdf is illustrated on the left-hand panel of Fig. 11. Equation (23) does not have any moments (i.e., the pdf does not fall off fast enough as a function of β to allow for, say, the mean and the variance to be computed). This implies that any estimator for its central value will be unreliable. The pdf for $\langle\beta\rangle$ estimated via Monte Carlo simulations has inherited these asymmetries; see the right-hand panel of Fig. 11. Because of the observed skewness, we expect the mean and the median to overestimate the anisotropy, especially for more negative $\beta*$ models, as was indeed seen in Fig. 10.

We are now in a position to discuss the inferred anisotropies of the Galactic Centre star cluster (Fig. 5 and Table 2) in more detail. Comparing with the distributions in Fig. 9, the evidence for radial anisotropy in the central 0.8 arcsec rests on the absence of stars with $\gamma_{TR} \simeq 1$, and the case for the tangential anisotropy of the He I stars on the absence of stars with $\gamma_{TR} \simeq -1$. Based on the Monte Carlo models, the evidence for anisotropy of the orbits is fairly solid. With larger proper motion samples, it may be best to compare with these distributions directly to estimate the anisotropy. The values for β estimated from equation (10), on the other hand, are quite uncertain. With this estimator being a quotient of observable dispersions, its distributions are very broad (Fig. 11). The Monte Carlo simulations indicate that a sample of 500 stars

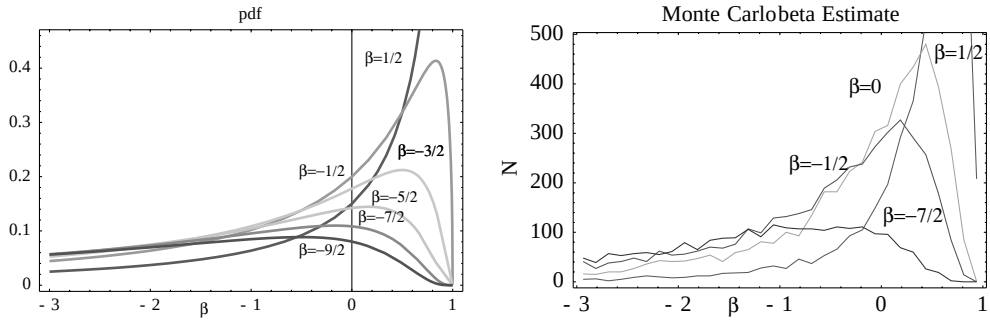

Figure 11. *Left-hand panel:* Theoretical β probability distribution (pdf) for $\beta_* = 1/2, -1/2 \cdots -9/2$ as labelled. These distributions are very skewed, and their means and standard deviations are ill-defined. *Right-hand panel:* Monte Carlo estimate of the probability distribution of $\hat{\beta}$ for models corresponding to $\beta_* = 1/2$, 0, $-1/2$ and $-7/2$. The distributions result from applying equation (10) to the values of $\langle v_R^2 \rangle$ and $\langle v_T^2 \rangle$ obtained for many random realizations of 20 stars from the respective star cluster models.

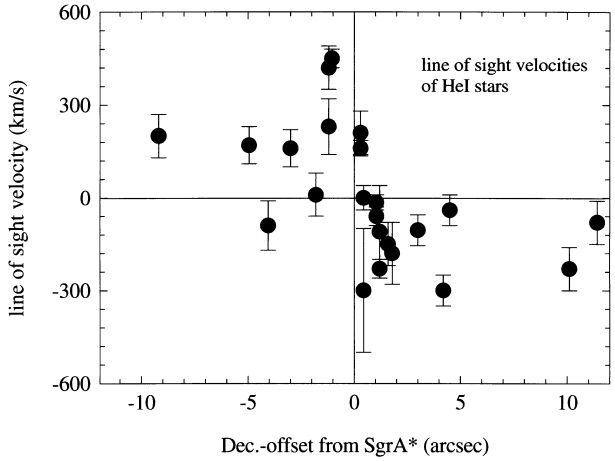

Figure 12. Line-of-sight velocities of all He I stars in Table 1, as a function of Dec.offset from SgrA*. Error bars are $\pm 1\sigma$.

with $v/\sigma(v)$ greater than 3 will be required in order to determine even $\beta_* = 1/2$ to an accuracy of ± 0.2.

In summary, the number of observed stars and the quality of the derived velocities are already sufficient to state with some certainty that anisotropies in the orbits of (early-type) stars are indeed present. To be consistent with the observed distribution of γ_{TR}, the model clusters (assuming sphericity and cylindrical symmetry of the velocity ellipsoid) require fairly strong radial anisotropy at small radii, and tangential anisotropy for larger radii. However, the data are not yet suited to place accurate quantitative constraints on the anisotropy parameter β and its radial dependence.

5 GLOBAL ROTATION OF THE EARLY-TYPE CLUSTER

As a group, the early-type stars (= the starburst component) exhibit a well-defined overall angular momentum. The line-of-sight velocities of the 29 emission-line stars follow a rotation pattern: blueshifted radial velocities north, and redshifted velocities south of the dynamic centre (Fig. 12). The apparent rotation axis is approximately east–west, within $\pm 20°$. The early-type stars are thus in a counter-rotation with respect to general Galactic rotation, the latter showing blueshifted material south and redshifted material north of the Galactic Centre. The rotation is fast (average $\approx 150\,\mathrm{km\,s^{-1}}$) and is consistent with a Keplerian boundary for a central mass of $(2–3) \times 10^6\,\mathrm{M_\odot}$ (Fig. 12). Our results confirm and improve the earlier conclusions of Genzel et al. (1996). Note that the late-type stars also show an overall rotation, but that is slow (a few tens of $\mathrm{km\,s^{-1}}$) and consistent with Galactic rotation (McGinn et al. 1989; Sellgren et al. 1990; Genzel et al. 1996; Haller et al. 1996).

Eckart & Genzel (1996) have argued that the He I stars also show a coherent pattern in their proper motions. Such a pattern is now confidently detected in the data (Fig. 13). It is the origin of much of the tangential anisotropy discussed above. 11 of the 13 proper motion vectors for the emission-line stars display a clockwise pattern, with only IRS 16NE and IRS 16NW moving counter-clockwise. A number of authors have argued that most of the members of the IRS 16 complex (located between SgrA* and 4 arcsec east of it, and between 3.5 arcsec south of SgrA* and 1.5 arcsec north of it) belong to the early-type cluster, with the He I stars just being a subsample of the brightest emission-line objects. This assertion is confirmed as well. Most of the brighter stars in the IRS 16 complex ($m_K \leq 13$) show a clockwise streaming pattern (Fig. 13, middle panel). In Fig. 13 (bottom panel) we overlay the proper motions vectors of Table 1 on the 0.05-arcsec-resolution K band Ghez et al. (1998) image of the SgrA* cluster. The preference of stars to be on radial/highly elliptical orbits that was discussed in the last section can be checked here from a graphical representation. Fig. 13 also suggests that the majority of stars in the SgrA* cluster have a similar projection of angular momentum along the line of sight, L_z, as the much brighter He I stars and the IRS 16 cluster members. Speckle spectrophotometry (Genzel et al. 1997) and very recent high-resolution VLT spectroscopy (Eckart, Ott & Genzel 1999) show that the brighter members of the SgrA* cluster lack 2.3–2.5 μm CO overtone absorption features, and are thus clearly not late-type stars. They are probably early-type stars. If they are on the main sequence, they would be of type B0 to B2. *The SgrA* cluster members thus are probably part of the early-type star cluster, but are on plunging, radial or very elliptical orbits*. The only alternative explanation of the observed radial anisotropies and net angular momentum is that the SgrA* cluster stars are rotating as a group, like the He I stars, but with a rotation axis lying in or near the plane of the sky. While this explanation seems relatively implausible, measurements of proper motion curvature and radial velocities are required to make a decisive test.

However, the early-type cluster cannot simply be modelled as an inclined, rotating thin disc. The fit of the best Keplerian disc model (inclination 40°, $v_{\mathrm{rot}} = 200\,r^{-0.5}$) to the He I star velocities

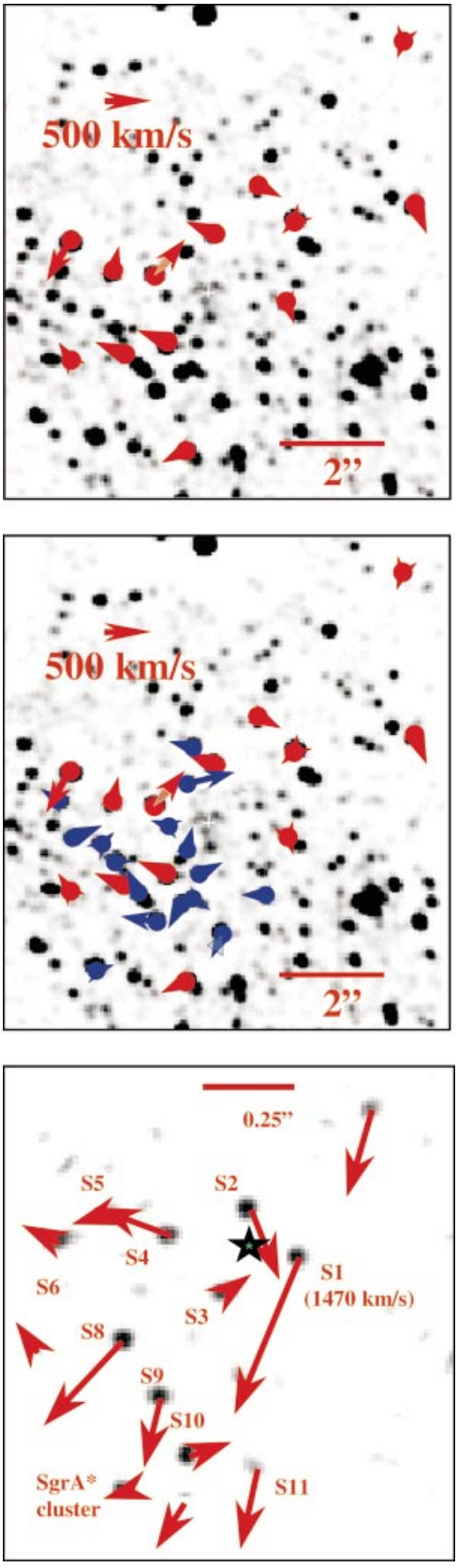

is poor. There are no He I stars seen at Galactocentric radii greater than ~12 arcsec. Because the He I stars should be phase-mixed along their orbits (Section 2.2), a better description of their distribution, and perhaps the entire early-type cluster, probably is a dynamically hot and geometrically thick, rotating torus at radii from 1 to 10 arcsec (0.039 to 0.39 pc).

Most of the stars in the torus will have a fairly large angular momentum L and approximately the same sign of L_z. In the distribution of different Ls there is a small fraction of stars, however, with much smaller L and still the same sign(L_z). This subpopulation is necessarily small and may thus not contain very massive stars. The low-L stars are able to pass much closer to SgrA* than the majority of the early-type star clusters. In our interpretation, it is these stars on largely radial, plunging orbits that make up the SgrA* cluster. As the bright, more massive stars are on average at larger distances from SgrA*, it is possible to detect fairly easily this central subsample of fainter, fast-moving stars. One would expect to find the same types of stars also at larger radii from SgrA*. However, the present proper motion data sets are biased against such fainter stars because of the presence of the brighter early-type stars (especially the IRS 16 cluster) and of late-type stars at yet larger true radii.

In summary of this section, we conclude that the majority of the He I emission-line stars and the bright (early-type) stars in the IRS 16 cluster show a coherent clockwise and counter-Galactic rotation. Their circular (tangential) velocities dominate over their radial velocities. The young stars are arranged in a thick torus of mean radius ≈0.2 pc. This torus was presumably first formed ≈7 to 9 million years ago when one or several infalling, tidally disrupted clouds collided and were highly compressed. This lead to an episode of active star formation in the central parsec. From the presence of bright AGB stars in the same region (Krabbe et al. 1995; Blum, Sellgren & dePoy 1996; Genzel et al. 1996) it is likely that there were other such phases of active star formation in the more distant past (a few hundred million years ago).

6 PROJECTED MASS ESTIMATOR AND ANISOTROPY

Leonard & Merritt (1989) have shown that an anisotropy-independent, projected mass estimator can be constructed from *radially* complete proper motion data. Starting from the Jeans

Figure 13. Proper motion vectors on K-band images of the central star cluster. North is up, and east is to the left. Top: proper motion vectors of all He I stars with three velocities, overlayed on a grey-scale SHARP map at 0.15-arcsec resolution. The length and direction of each arrow denote the magnitude and direction of the proper motion for each star. For comparison, a 500 km s^{-1} motion (for $R_\odot = 8.0$ kpc) is shown in the upper left. To indicate the uncertainties in direction for the best stars, a shaded cone is shown for IRS 16C. The white cross denotes the location of SgrA*. The middle panel shows in addition the vectors for all stars in the IRS 16 complex that have K-magnitudes ≤13. This criterion probably selects primarily early-type stars. Proper motion vectors within ≈0.7 arcsec of SgrA* (the 'SgrA* cluster'), overlayed on the 0.05-arcsec resolution K-band map of Ghez et al. (1998), are given in the bottom panel. The asterisk marks the position of SgrA*. The 1σ positional uncertainty of the radio source on the infrared map is between ±10 and ±30 milli-arseconds (1σ). The identifications of the sources (S1–S11, Table 1) are given. The length of the proper motion of S1 corresponds to 1470 km s^{-1} for $R_\odot$ = 8.0 kpc.

equation for a spherically symmetric, non-rotating system,

$$GM(r) = -r\sigma_r^2[\mathrm{d}\log n(r)/\mathrm{d}\log r + \mathrm{d}\log \sigma_r^2/\mathrm{d}\log r + 2(1-\sigma_t^2/\sigma_r^2)], \quad (24)$$

one can construct the spatially averaged, stellar tracer density $[n(r)]$ weighted expectation value $G\langle M(r)\rangle$. This estimator, henceforth referred to as the Leonard–Merritt (LM) estimator, is independent of any assumptions about anisotropy,

$$G\langle M(r)\rangle_{\mathrm{LM}} = \langle r(2\sigma_r^2 + 2\sigma_t^2)\rangle = (16/3\pi)(2\langle R\sigma_R^2\rangle + \langle R\sigma_T^2\rangle). \quad (25)$$

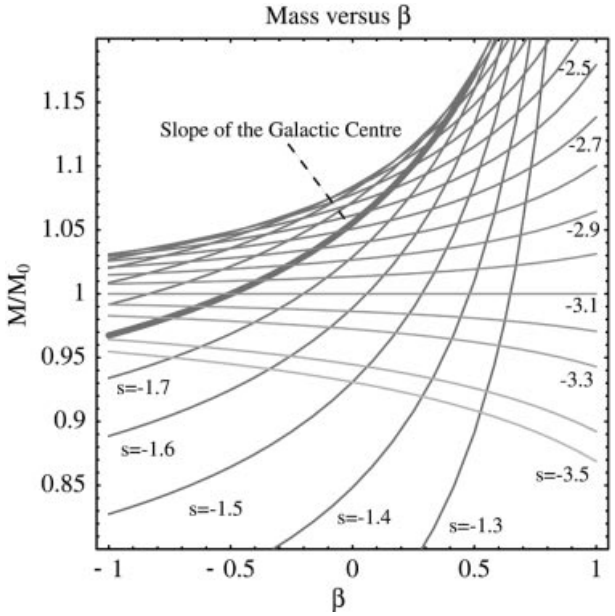

Figure 14. Leonard–Merritt mass estimates (in units of the true underlying mass) as a function of β for different power-law slopes of clusters as labelled (the thicker curve corresponds to $\rho \propto r^{-1.8}$). Note that for all power-law clusters, except that corresponding to $\rho \propto r^{-3}$, the mass estimate is typically biased and gives an overestimate or underestimate of the real mass. In particular, note that the Bahcall–Tremaine estimate (corresponding to $\beta = 0$) is also offset for all slopes except 3 and 1.62. For instance, for $\beta = 0$ and $\rho \propto r^{-1.8}$ the relative mass discrepency reads $M_{\mathrm{LM}}/M_0 \approx 1.05$, but for $\beta = -5$ it reaches $\approx$0.89, while a purely radial cluster would lead to an overestimation of 60 per cent, as shown in Table 3. In practice, our estimate of the mass of the black hole should be rescaled downward by about 5–10 per cent to account for this bias in the relevant radial range.

Table 2 lists the LM estimator obtained from 95 proper motion stars within 5 arcsec of SgrA*. The estimated mass is $(2.9 \pm 0.4) \times 10^6\,\mathrm{M}_\odot$. It is quite insensitive to the weighting scheme of the data. We also list LM estimates for different projected annuli (although this is formally not appropriate; see below).

For comparison, the Bahcall–Tremaine (1981, hereafter BT) estimator for an isotropic cluster around a point mass gives a mass of $(3.1 \pm 0.3) \times 10^6\,\mathrm{M}_\odot$ for the 2×95 proper motions within $R =$ 5 arcsec (Table 2). For purely radial orbits the mass would be twice as large. Note, however, that formally the BT estimator is defined for radial velocities only, and as such the application to proper motions is inappropriate. The virial theorem (VT) mass estimate of the same data gives $(2.5\text{–}2.6) \times 10^6\,\mathrm{M}_\odot$ (Table 2; see Bahcall & Tremaine 1981 or Genzel et al. 1996 for a discussion). The BT estimator requires prior knowledge of the orbit structure. In the region outside 3 arcsec from SgrA*, where from our proper motion analysis the orbit structure is approximately isotropic, the agreement between all three estimators is fair (at somewhat more than 1σ).

6.1 Correction for the Leonard–Merritt mass estimate

Unfortunately, the LM mass estimate assumes that the cluster is of finite mass and that we have access to the full radial extent of the cluster. Here the density profile behaves roughly as a power law over the finite range of radii for which data are available. For such a mass model in a Keplerian potential the implementation of the LM mass estimate on concentric rings yields a biased (systematically offset) measure of the mass. Indeed, the derivation of this estimator involves an integration by part of integrals of the form

$$\int_0^\infty r^4 \frac{\mathrm{d}\rho\sigma^2(r)}{\mathrm{d}r}\,\mathrm{d}r = -4\int_0^\infty \rho(r) r^3 \sigma^2(r)\,\mathrm{d}r + [\rho(r) r^4 \sigma^2(r)]_0^\infty. \quad (26)$$

For finite-mass systems the second term of the right-hand side of equation (26) vanishes. In the context of the Galactic Centre we still compute

$$\int_{r_1}^{r_2} \rho(r) r^3 \sigma^2(r)\,\mathrm{d}r \Big/ \int_{r_1}^{r_2} \rho(r) r^2 \sigma^2(r)\,\mathrm{d}r \quad (27)$$

Table 3. Correction factor M_{LM}/M_0 for LM mass estimator versus β (horizontally) and s (vertically). Note the steep rise near $\beta = 1$ for shallower density profiles. The function $(M_{\mathrm{LM}}/M_0)(\beta,s)$ is illustrated in Fig. 14.

$s\backslash\beta$	−5	−4	−3	−2	−1	0	0.25	0.5	0.75	1
−1.2	0.43	0.43	0.44	0.46	0.49	0.57	0.62	0.71	0.93	2.3
−1.4	0.67	0.67	0.69	0.71	0.75	0.85	0.91	1.	1.2	2.
−1.5	0.74	0.75	0.77	0.79	0.83	0.93	0.99	1.1	1.3	1.9
−1.6	0.81	0.81	0.83	0.85	0.89	0.99	1.	1.1	1.3	1.8
−1.7	0.85	0.86	0.88	0.9	0.93	1.	1.1	1.2	1.3	1.7
−1.8	0.89	0.9	0.91	0.93	0.97	1.1	1.1	1.2	1.3	1.6
−1.9	0.92	0.93	0.94	0.96	0.99	1.1	1.1	1.2	1.3	1.5
−2.	0.94	0.95	0.96	0.98	1.	1.1	1.1	1.2	1.3	1.4
−2.2	0.97	0.98	0.99	1.	1.	1.1	1.1	1.1	1.2	1.3
−2.4	0.99	1.	1.	1.	1.	1.1	1.1	1.1	1.2	1.2
−2.5	1.	1.	1.	1.	1.	1.1	1.1	1.1	1.1	1.2
−2.6	1.	1.	1.	1.	1.	1.1	1.1	1.1	1.1	1.1
−2.8	1.	1.	1.	1.	1.	1.	1.	1.	1.	1.1
−3.	1.	1.	1.	1.	1.	1.	1.	1.	1.	1.
−3.5	0.98	0.98	0.98	0.97	0.95	0.93	0.92	0.91	0.89	0.87

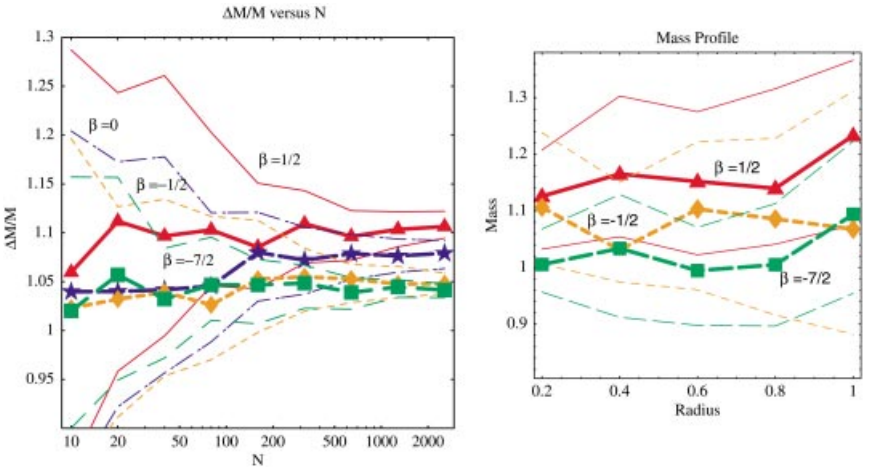

Figure 15. *Left-hand panel:* Median and quartiles for the distribution of values for the mass estimator $M_{\rm LM}$ (equation 10) from simulated proper motion samples, as a function of sample size and for several underlying anisotropy values $\beta_* = 0.5, 0, -0.5, -3.5$ of the simulated star cluster. The true central mass is unity, and the offset induced by the LM estimation is clearly visible there and in accordance with the theoretical prediction from Table 6. Mass determinations reliable at the 10 per cent level require samples of at least 40, 35, 25 and 15 stars for $\beta_* = 0.5, 0, -0.5$ and -3.5. *Right-hand panel:* Central mass estimates $M_{\rm LM}$ derived in five annuli on the sky for a total number of 800 stars. Anisotropy values are $\beta_* = 0.5, -0.5$ and -3.5, as labelled (plain, dash-dot, long dash, dash) corresponding to (triangle, star, diamond, square).

Table 4. Surface densities and line-of-sight velocity dispersions.

Projected distance from SgrA* (arcsec)	$m(K) < 15$ source surface density Σ sources per square arcsec	$2\Delta\Sigma/\Sigma$	
0.5	3.5	0.3	
1.5	2.4	0.3	
2.5	2.2	0.25	
4	1.55	0.3	
6	1.06	0.2	
8.5	1	0.2	
11.5	0.57	0.2	
16.5	0.57	0.3	
23	0.44	0.3	
28.8	0.27	0.32	
34.1	0.22	0.4	
73	0.14	0.4	
114.1	0.08	0.6	
Projected distance from SgrA* (arcsec)	σ_z (km s^{-1})	$2\Delta(\sigma_z)/\sigma_z$ (km s^{-1})	Stellar type
2.2	195	0.35	He I
8.5	164	0.9(a)	He I
8.7	102	0.15	late-type
10	99	0.21	late-type
17.3	72	0.15	late-type
20	85	0.35	late-type
32	68	0.38	late-type
100	54	0.22	late-type

(a) Given low weight to de-emphasize the dominant rotation signal of the early-type stars at this radius.

over a finite radial range r_1,r_2, and even though both numerator and denominator diverge as $r_1 \to 0$ and $r_1 \to \infty$, the ratio is well defined and equals the value corresponding to finite r_1 and r_2. On the other hand,

$$[\rho(r)r^4\sigma^2(r)]_{r_1}^{r_2} / \int_{r_1}^{r_2} \rho(r)r^2\sigma^2(r)\,{\rm d}r \tag{28}$$

is also finite but non-zero except for $s = -3$. As a consequence, the ratio $M_{\rm LM}/M_0$ will typically be a function of β and s, the slope of the local power law corresponding to the range for which data are available. A straightfoward calculation yields

$$\frac{M_{\rm LM}}{M_0} = \frac{2^{4+s}\Gamma(-s/2)((3-s)(1-s-\beta)\Gamma(-s) - \Gamma(2-s))}{3\sqrt{\pi}(1-s-2\beta)\Gamma(-s/2-1/2)\Gamma(1/2-s/2)\Gamma(3/2-s/2)}. \tag{29}$$

Relevant relative mass estimates versus β for different power-law index are shown in Fig. 14. In practice, equation (29) is used to correct for the offset in the measured $M_{\rm LM}$. Table 3 gives a few values relevant for the Galactic Centre.

Table 5. Best Jeans mass model including anisotropy (for 8.0 kpc).

$n(0)$	$r(0)$	α_r	χ^2/N		
3.4	1.25"	1.8	0.83		
$\sigma_r[r(0)]$	$\alpha_{\sigma r}$	$\sigma_t(r(0))$	$\alpha_{\sigma t}$	σ_0	
280 km s^{-1}	1	353 km s^{-1}	0.5	50 km s^{-1}	
r (pc)	$\mathrm{d}\log n/\mathrm{d}\log r$	$\mathrm{d}\log\sigma^2/\mathrm{d}\log r$	$2\beta(r)$	$M(\mathrm{M}_\odot)$	$2\Delta M/M$
1.02E−02	−1.03E−01	−2.00E+00	1.33E+00	3.25E+06	7.50E−01
1.06E−02	−1.09E−01	−2.00E+00	1.30E+00	3.26E+06	7.00E−01
1.10E−02	−1.17E−01	−2.00E+00	1.27E+00	3.28E+06	6.50E−01
1.15E−02	−1.25E−01	−2.00E+00	1.24E+00	3.29E+06	6.50E−01
1.19E−02	−1.33E−01	−1.99E+00	1.21E+00	3.29E+06	6.00E−01
1.24E−02	−1.43E−01	−1.99E+00	1.18E+00	3.30E+06	6.00E−01
1.29E−02	−1.53E−01	−2.00E+00	1.15E+00	3.33E+06	5.50E−01
1.35E−02	−1.64E−01	−2.00E+00	1.11E+00	3.34E+06	5.50E−01
1.40E−02	−1.74E−01	−1.99E+00	1.08E+00	3.35E+06	5.50E−01
1.46E−02	−1.85E−01	−1.99E+00	1.04E+00	3.36E+06	5.00E−01
1.52E−02	−1.98E−01	−1.99E+00	9.99E−01	3.38E+06	5.00E−01
1.58E−02	−2.11E−01	−1.99E+00	9.58E−01	3.39E+06	5.00E−01
1.64E−02	−2.24E−01	−1.99E+00	9.16E−01	3.41E+06	4.70E−01
1.71E−02	−2.40E−01	−1.99E+00	8.72E−01	3.42E+06	4.50E−01
1.78E−02	−2.55E−01	−1.99E+00	8.26E−01	3.44E+06	4.30E−01
1.85E−02	−2.70E−01	−1.99E+00	7.78E−01	3.45E+06	4.20E−01
1.93E−02	−2.88E−01	−1.99E+00	7.28E−01	3.46E+06	4.10E−01
2.01E−02	−3.06E−01	−1.99E+00	6.76E−01	3.48E+06	4.00E−01
2.09E−02	−3.24E−01	−1.99E+00	6.22E−01	3.49E+06	4.00E−01
2.17E−02	−3.44E−01	−1.99E+00	5.66E−01	3.50E+06	3.90E−01
2.26E−02	−3.64E−01	−1.99E+00	5.08E−01	3.51E+06	3.80E−01
2.36E−02	−3.86E−01	−1.98E+00	4.48E−01	3.53E+06	3.70E−01
2.45E−02	−4.08E−01	−1.98E+00	3.85E−01	3.54E+06	3.60E−01
2.55E−02	−4.31E−01	−1.98E+00	3.19E−01	3.55E+06	3.50E−01
2.66E−02	−4.55E−01	−1.98E+00	2.51E−01	3.56E+06	3.40E−01
2.76E−02	−4.80E−01	−1.98E+00	1.80E−01	3.57E+06	3.30E−01
2.88E−02	−5.06E−01	−1.98E+00	1.07E−01	3.58E+06	3.20E−01
2.99E−02	−5.33E−01	−1.98E+00	3.04E−02	3.59E+06	3.10E−01
3.12E−02	−5.60E−01	−1.97E+00	−4.89E−02	3.60E+06	3.00E−01
3.24E−02	−5.88E−01	−1.97E+00	−1.31E−01	3.61E+06	3.00E−01
3.38E−02	−6.17E−01	−1.97E+00	−2.17E−01	3.61E+06	2.90E−01
3.51E−02	−6.46E−01	−1.97E+00	−3.06E−01	3.62E+06	2.80E−01
3.66E−02	−6.76E−01	−1.96E+00	−3.98E−01	3.63E+06	2.70E−01
3.81E−02	−7.08E−01	−1.96E+00	−4.94E−01	3.63E+06	2.70E−01
3.96E−02	−7.39E−01	−1.96E+00	−5.93E−01	3.64E+06	2.60E−01
4.12E−02	−7.69E−01	−1.95E+00	−6.96E−01	3.64E+06	2.60E−01
4.29E−02	−8.01E−01	−1.95E+00	−8.03E−01	3.64E+06	2.50E−01
4.47E−02	−8.33E−01	−1.95E+00	−9.13E−01	3.64E+06	2.50E−01
4.65E−02	−8.66E−01	−1.94E+00	−1.03E+00	3.64E+06	2.40E−01
4.84E−02	−8.99E−01	−1.94E+00	−1.15E+00	3.64E+06	2.40E−01
5.04E−02	−9.31E−01	−1.93E+00	−1.27E+00	3.64E+06	2.30E−01
5.24E−02	−9.63E−01	−1.93E+00	−1.40E+00	3.64E+06	2.30E−01
5.46E−02	−9.96E−01	−1.92E+00	−1.53E+00	3.63E+06	2.20E−01
5.68E−02	−1.03E+00	−1.91E+00	−1.66E+00	3.63E+06	2.20E−01
5.91E−02	−1.06E+00	−1.91E+00	−1.80E+00	3.62E+06	2.10E−01
6.15E−02	−1.09E+00	−1.90E+00	−1.95E+00	3.62E+06	2.10E−01
6.40E−02	−1.12E+00	−1.90E+00	−2.09E+00	3.61E+06	2.10E−01
6.66E−02	−1.15E+00	−1.89E+00	−2.25E+00	3.60E+06	2.10E−01
6.93E−02	−1.18E+00	−1.88E+00	−2.40E+00	3.60E+06	2.00E−01
7.22E−02	−1.21E+00	−1.87E+00	−2.57E+00	3.59E+06	2.00E−01
7.51E−02	−1.24E+00	−1.86E+00	−2.73E+00	3.58E+06	2.00E−01
7.82E−02	−1.27E+00	−1.85E+00	−2.90E+00	3.57E+06	2.00E−01
8.14E−02	−1.29E+00	−1.84E+00	−3.08E+00	3.56E+06	2.00E−01
8.47E−02	−1.32E+00	−1.82E+00	−3.25E+00	3.55E+06	2.00E−01
8.82E−02	−1.34E+00	−1.81E+00	−3.44E+00	3.54E+06	2.00E−01
9.18E−02	−1.37E+00	−1.79E+00	−3.62E+00	3.53E+06	2.00E−01
9.55E−02	−1.39E+00	−1.78E+00	−3.81E+00	3.52E+06	2.00E−01
9.94E−02	−1.41E+00	−1.76E+00	−4.00E+00	3.51E+06	2.00E−01
1.03E−01	−1.43E+00	−1.75E+00	−4.20E+00	3.50E+06	2.00E−01
1.08E−01	−1.45E+00	−1.73E+00	−4.39E+00	3.49E+06	2.00E−01
1.12E−01	−1.47E+00	−1.71E+00	−4.59E+00	3.48E+06	2.00E−01
1.17E−01	−1.49E+00	−1.69E+00	−4.79E+00	3.47E+06	2.00E−01
1.21E−01	−1.51E+00	−1.67E+00	−4.99E+00	3.46E+06	2.00E−01
1.26E−01	−1.53E+00	−1.64E+00	−5.19E+00	3.45E+06	2.00E−01
1.32E−01	−1.54E+00	−1.62E+00	−5.39E+00	3.44E+06	2.00E−01

Table 5 – *continued*

r (pc)	$\mathrm{d}\log n/\mathrm{d}\log r$	$\mathrm{d}\log\sigma^2/\mathrm{d}\log r$	$2\beta(r)$	$M(\mathrm{M}_\odot)$	$2\Delta M/M$
1.37E−01	−1.56E+00	−1.60E+00	−5.58E+00	3.43E+06	2.00E−01
1.42E−01	−1.57E+00	−1.57E+00	−5.78E+00	3.42E+06	2.00E−01
1.48E−01	−1.59E+00	−1.54E+00	−5.97E+00	3.41E+06	2.00E−01
1.54E−01	−1.60E+00	−1.51E+00	−6.16E+00	3.41E+06	2.00E−01
1.61E−01	−1.61E+00	−1.48E+00	−6.34E+00	3.40E+06	2.00E−01
1.67E−01	−1.62E+00	−1.45E+00	−6.52E+00	3.39E+06	2.00E−01
1.74E−01	−1.64E+00	−1.42E+00	−6.70E+00	3.39E+06	2.00E−01
1.81E−01	−1.65E+00	−1.38E+00	−6.86E+00	3.38E+06	2.00E−01
1.89E−01	−1.66E+00	−1.35E+00	−7.02E+00	3.38E+06	2.00E−01
1.96E−01	−1.67E+00	−1.31E+00	−7.16E+00	3.37E+06	2.10E−01
2.04E−01	−1.67E+00	−1.28E+00	−7.30E+00	3.37E+06	2.11E−01
2.13E−01	−1.68E+00	−1.24E+00	−7.43E+00	3.37E+06	2.20E−01
2.21E−01	−1.69E+00	−1.20E+00	−7.54E+00	3.36E+06	2.30E−01
2.30E−01	−1.70E+00	−1.16E+00	−7.64E+00	3.36E+06	2.40E−01
2.40E−01	−1.70E+00	−1.12E+00	−7.74E+00	3.36E+06	2.50E−01
2.49E−01	−1.71E+00	−1.08E+00	−7.81E+00	3.36E+06	2.60E−01
2.60E−01	−1.72E+00	−1.04E+00	−7.87E+00	3.36E+06	2.60E−01
2.70E−01	−1.72E+00	−1.00E+00	−7.92E+00	3.36E+06	2.70E−01
2.81E−01	−1.73E+00	−9.65E−01	−7.96E+00	3.36E+06	2.70E−01
2.93E−01	−1.73E+00	−9.25E−01	−7.98E+00	3.37E+06	2.80E−01
3.05E−01	−1.74E+00	−8.85E−01	−7.98E+00	3.37E+06	2.80E−01
3.17E−01	−1.74E+00	−8.46E−01	−7.98E+00	3.38E+06	2.80E−01
3.30E−01	−1.74E+00	−8.07E−01	−7.95E+00	3.38E+06	2.90E−01
3.43E−01	−1.75E+00	−7.69E−01	−7.92E+00	3.39E+06	2.90E−01
3.58E−01	−1.75E+00	−7.32E−01	−7.87E+00	3.39E+06	3.10E−01
3.72E−01	−1.76E+00	−6.95E−01	−7.81E+00	3.40E+06	3.30E−01
3.87E−01	−1.76E+00	−6.59E−01	−7.73E+00	3.41E+06	3.50E−01
4.03E−01	−1.76E+00	−6.24E−01	−7.65E+00	3.42E+06	3.70E−01
4.20E−01	−1.76E+00	−5.91E−01	−7.55E+00	3.43E+06	3.90E−01
4.37E−01	−1.77E+00	−5.58E−01	−7.45E+00	3.44E+06	4.10E−01
4.54E−01	−1.77E+00	−5.26E−01	−7.34E+00	3.45E+06	4.30E−01
4.73E−01	−1.77E+00	−4.96E−01	−7.21E+00	3.47E+06	4.50E−01
4.92E−01	−1.77E+00	−4.66E−01	−7.08E+00	3.48E+06	5.00E−01

Note that $M_{\mathrm{LM}} = M_0$ for $\beta = 0$ when s is -3 or the root of

$$16\Gamma(s/2)\left((1-s)(3-s)\Gamma(s) - \Gamma(2-s)\right) = 32^{1-s}\sqrt{\pi}\Gamma(-s/2-1/2)\Gamma(3/2-s/2)^2, \quad (30)$$

which yields $s \approx -1.62$. More generally, there is a non-trivial curve (i.e., which differs from $s = -3$) corresponding to $M_{\mathrm{LM}}/M_0 = 1$ in the (β,s) plane.

We conclude that the LM estimator is not independent of β or s when applied to truncated data set even though each shell yields the same mass estimate for a Keplerian potential. We do need to estimate β and s independently to correct for the offset. Since β varies with radius for the Galactic Centre, the correction will affect the mass profile.

The mass estimators are derived by averaging over the entire star cluster, while the observed stars in the Galactic Centre are presumably part of a more extended stellar system. To test for possible systematic effects, we have therefore also carried out Monte Carlo simulations for the LM estimator. Again, as in Section 4.2, we have used a power-law distribution of tracer stars with $n \propto r^{-2.5}$ as for the kinematically measured stars. The left-hand panel of Fig. 15 shows the median and quartiles of the distribution of M_{LM} values derived for many star cluster realizations, as a function of sample size and for $\beta_* = 0.5, 0, -0.5$ and -3.5. The true mass of the central black hole that dominates the potential of these clusters is $M = 1$. The right-hand panel of Fig. 15 shows, for $N = 800$ stars, the effect of estimating the central mass from five concentric annuli aranged linearly as a function of radius. Note that the mass profile is indeed flat (within the statistical uncertainties), as expected for a Keplerian potential and offset by the amount predicted by equation (29).

These simulations suggest that applying the LM estimator to a central subvolume of the actual star cluster around the black hole gives the correct hole mass if the distribution of orbits is strongly tangential, independent of power-law slope (all radial shells should then be independently sufficient). For isotropic and radially anisotropic orbit distributions and power-law slopes near -2 the LM estimator gives somewhat biased (too high) values for the central mass. The value of $M = 2.9 \times 10^6\,\mathrm{M}_\odot$ derived for the central mass from all stars inside 5 arcsec (an approximately overall isotropic sample) is thus probably systematically high by about 5–10 per cent.

6.2 Estimate of the Sun–Galactic Centre distance $R_\odot$

The expectation values of the first moments of the projected velocity dispersions are related to each other through their mutual dependence on the intrinsic radial and tangential velocity dispersions. One can write

$$\langle R\sigma_z^2\rangle = (1/3)\langle R\sigma_R^2\rangle + (2/3)\langle R\sigma_T^2\rangle. \quad (31)$$

The z-velocity is determined directly through the Doppler shifts of the stars. The R- and T-velocities depend on the assumed Sun–Galactic Centre distance $R_\odot$. For a spatially and kinematically spherical system it is therefore possible to derive the distance to the Galactic Centre from equation (31), without any prior assumptions on the anisotropy. The relationship is

$$(R_\odot/8\,\mathrm{kpc}) = [\langle R\sigma_z^2\rangle_8/(1/3\langle R\sigma_R^2\rangle_8 + 2/3\langle R\sigma_T^2\rangle_8)]^{0.5}. \quad (32)$$

Here $\langle\,\rangle_8$ refers to the values calculated under the assumption that the Galactic Centre distance is 8.0 kpc, as assumed for the proper motions in Table 1. Taking only those 32 stars for which we have all three velocity components, we find $R_\odot = 8.95 \pm 1.6$ kpc. Taking all 104 proper motion stars within $R \leq 8.8$ arcsec and all 71 stars with z-velocities within the same projected radius, we find $R_\odot = 8.2 \pm 0.9$ kpc. The specific moment analysis in equation (32) as applied to these samples is appropriate if the motions are completely dominated by a central point mass. In that case, $R\sigma^2 \approx$ constant and data points at different R (but the same quality) are appropriately given the same weight. In the Galactic Centre the mass distribution is a sum of a central point mass and a near-isothermal stellar cluster of velocity dispersion $\sigma_0 = 50$ to 55 km s^{-1} derived from the stellar velocities outside the sphere of influence of the black hole (Genzel et al. 1996). It may thus be more appropriate to subtract σ_0^2 before computing the expectation values in equations (26) and (27). In that case we obtain $R_\odot = 7.9 \pm 0.85$ kpc. The difference between these two last estimates arises since the line-of-sight velocity data are biased to a larger $\langle R\rangle$ than the proper motions, so that the effect of removing σ_0 has a larger impact on the z-velocities. This differentially decreases slightly the distance estimate relative to that obtained for $\sigma_0 = 0$. All errors do not contain a possible systematic term from deviations from spherical symmetry.

Our analysis is in excellent agreement with other recent estimates for the Galactic Centre distance which range between 7.2 and 9.0 kpc with a best weighted average of 8.0 ± 0.5 kpc (see the review by Reid 1993). The statistical uncertainty of our estimate rivals the best other methods available for determining $R_\odot$: cluster parallaxes through H_2O maser proper motions, global modelling of the Galaxy, globular cluster dynamics, RR Lyrae stars, Cepheids, planetary nebulae and OB stars in H II regions (Reid 1993) and clump giant stars (Paczynski & Stanek 1998).

7 JEANS MODELLING OF THE CENTRAL MASS DISTRIBUTION

We have also carried out a full Jeans modelling of the data set, explicitly allowing for the anisotropy term in equation (24). It is clear that the number of stars is still too small to determine unambiguously the radial profiles of anisotropy and mass for all different stellar components (and including rotation). Here we give only a simplified overall model which is consistent with all the data. Our model proceeds from a parametrized Ansatz for the different quantities, as described earlier in Genzel et al. (1996),

$$n(r) = 2n_0/\{\pi r_0[1 + (r/r_0)^{\alpha_r}]\}, \quad \sigma_r^2(r) = \sigma_{r0}^2(r/r_0)^{-2\alpha_{\sigma r}} + \sigma_0^2$$

$$\text{and} \quad \sigma_t^2(r) = \sigma_{t0}^2(r/r_0)^{-2\alpha_{\sigma t}} + \sigma_0^2. \qquad (33)$$

To compare to the observed surface density distribution $\Sigma(R)$, and observed velocity dispersions $\sigma_z(R)$, $\sigma_R(R)$ and $\sigma_T(R)$, the expressions in equation (33) were numerically integrated along the line of sight and weighted with the density distribution, as described in equations (5) and (6). The data were averaged in annuli centred around SgrA* to yield 13 values for $\Sigma(R)$ between $R = 0.5$ and 114 arcsec, eight values for $\sigma_z(R)$ between $R = 2$ and 100 arcsec, and five values each for $\sigma_R(R)$ and $\sigma_T(R)$ between $R = 0.4$ and 7.3 arcsec. Best-fitting values for the eight parameters in the expressions above were then determined from a χ^2 minimization. They are listed in Table 5. The surface density measurements come from number counts with the SHARP speckle camera to $m(K) = 15$, and are corrected for crowding and incompleteness (Schmitt 1995). The data points and their statistical errors are listed in Table 4. The R- and T-velocity dispersion values are from Table 2. The line-of-sight-velocity dispersions are listed in Table 4 as well. The two data points at $R = 2.2$ and 8.5 arcsec are derived from the He I star velocities in Table 1. In addition, we have taken late-type star velocity dispersions from Genzel et al. (1996) and references therein. The 13 surface density measurements in Table 4 constrain the three parameters of the density distribution given in equation (33) very well. Likewise the 18 velocity dispersion measurements also give good constraints on the five parameters of the dispersion expressions in equation (33).

Fig. 16 shows the surface density and velocity data, along with the best-fitting model whose parameters are given in Table 5. Table 5 also lists the best anisotropic mass model, along with the logarithmic gradients and the β-anisotropy parameter that were used in the Jeans equation (equation 24) to derive that mass model.

8 DISCUSSION AND CONCLUSIONS

The connected black crosses in Fig. 17 depict the mass distribution obtained from the Jeans model with anisotropy (and its 1σ uncertainty). For comparison, we also show the LM-mass estimators from Table 2, BT estimators for the z- and proper motions (this paper; Genzel et al. 1996, 1997; Ghez et al. 1998), the isotropic Jeans mass model of Genzel et al. (1996), and a few of the mass estimates determined from the gas motions (Serabyn & Lacy 1985; Güsten et al. 1987; Lacy, Achtermann & Serabyn 1991; Herbst et al. 1993; Roberts & Goss 1993). The mass inside of the innermost bin ($r = 0.01$pc) of our best Jeans model is 3.25×10^6 M$_\odot$. It is consistent with the LM mass estimator of the entire proper motion sample inside 5 arcsec, $M_{\rm LM} = 2.9 \pm 0.4 \times 10^6$ M$_\odot$ (Table 2; see also Section 6). When corrected for the bias discussed above, that mass becomes about $(2.6\text{–}2.8) \times 10^6$ M$_\odot$. Systematic effects and the method of modelling dominate the accuracy to which the central mass can be determined. In Fig. 17 we plot a central mass of 3.0×10^6 M$_\odot$. This value is a compromise between the bias-corrected LM estimate and the Jeans estimate. Its overall (systematic plus statistical) uncertainty is $\pm 0.5 \times 10^6$ M$_\odot$. It is reassuring that the results of our simple anisotropic modelling and of previous isotropic models are in good agreement within the respective errors. *Our results confirm that the mass distribution is flat between* 0.01 *and* 0.5 pc.

None the less, there are still significant uncertainties in this analysis.

(i) The parametric form of the model fitted to the data is not unique.

(ii) We have so far not distinguished between early- and late-type stars. Yet it is fairly clear that early- and late-type stars have different spatial distributions and kinematics (see plate 1 in Genzel et al. 1996). In the Jeans analysis, we require the density distribution and kinematics of an equilibrium tracer population. The proper motions stars are heavily influenced by spatial selection biases; thus it is not appropriate to use their inferred number density distribution in the Jeans equation. Their role is to provide local velocity measurements for the population that they represent. The early-type stars contribute much to these kinematic measurements; if they are more centrally concentrated than the overall population measured by the SHARP number counts, this will have the effect of underestimating the central mass.

(iii) The version of the Jeans equation we have used in

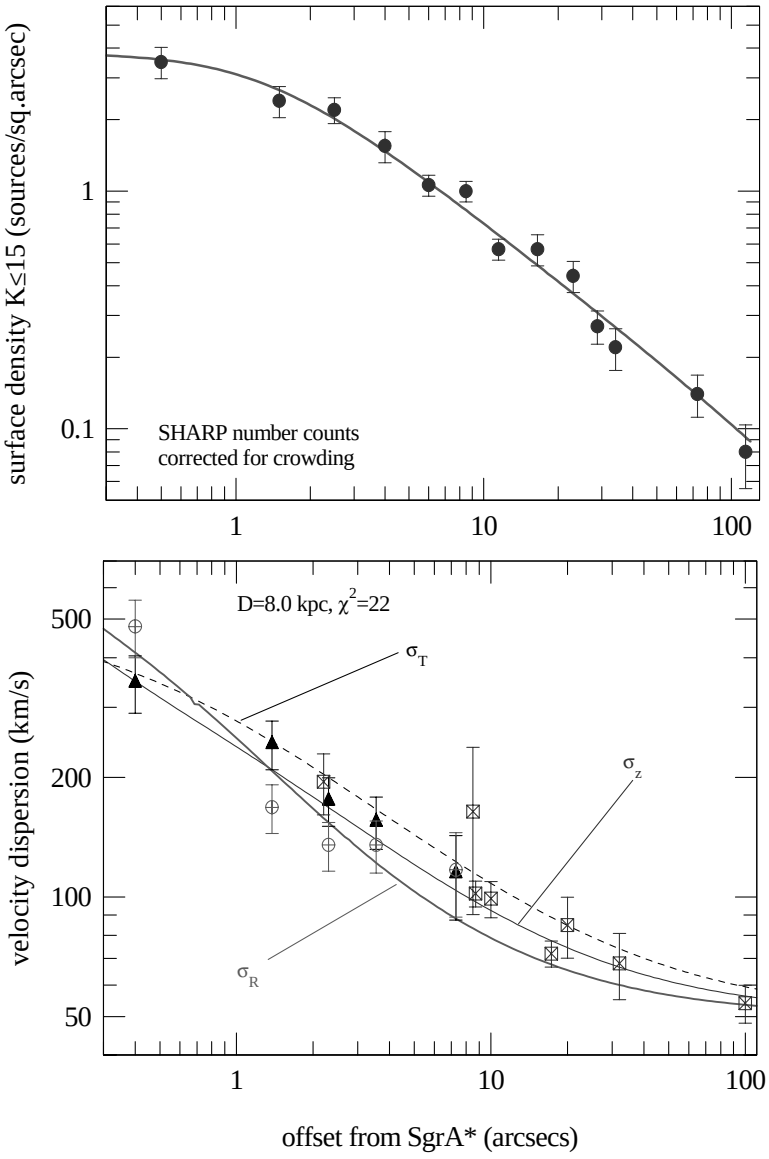

Figure 16. Surface density and velocity dispersions as a function of projected separation from SgrA*, along with the best-fitting anisotropic Jeans model described in section 7. The observed $m(K) \leq 15$ surface density counts, and their 1σ uncertainties, are shown in the top panel (see also Table 4). These counts come from Schmitt (1995) and have been corrected for the effects of crowding and bright stars. The continuous curve is the model of equation (33) with the parameters in Table 5, integrated along the line of sight as described in equations (5) and (6). The bottom panel shows observations of the projected tangential velocity dispersions (*T*: triangles, this paper, Table 2), projected radial velocity dispersions (*R*: circles, this paper, Table 2) and line-of-sight-velocity dispersions (*z*: rectangles with crosses, Table 4). The data for the line-of-sight dispersions come from this paper (He I stars), and from Genzel et al. (1996), Haller et al. (1996), Lindqvist et al. (1992), Sellgren et al. (1990) and McGinn et al. (1989). The best anisotropic Jeans model integrated along the line of sight (Table 5) gives the black, thin dashed curve for the projected tangential (*T*) data points, the thick continuous curve (red in the colour version of the figure reproduced in *Synergy*) for the projected radial (*R*) data points and the thin continuous curve (blue in the colour version of the figure reproduced in *Synergy*) for the line-of-sight (*z*) data points. The model assumes a distance of 8 kpc and gives a total χ^2 of 21.6, or a reduced χ^2/N of 0.83.

expression (24) neglects rotation. However, we have discussed above the strong evidence for coherent motion of the He I star cluster. The late-type stars have only a small overall rotation. Including rotation and distinguishing in the analysis between late and early-type stars would thus be desirable (as in Genzel et al. 1996 for the isotropic case). Unfortunately, this is not possible, because of the large number of free parameters (three more for density distribution, and approximately eight more for velocity distribution) and the relatively poor constraints on a number of the parameters. There are no early-type stars outside 11 arcsec, there are very few late-type stars inside 5 arcsec, and the accuracy of the proper motion *R*- and *T*-velocity dispersions is low if all proper motions without a stellar type identification are discarded. We have run models with explicit inclusion of rotation but found it to be overall a poorer fit than the models without rotation. To deliberately de-emphasize the rotation signature of the He I star cluster, we have arbitrarily given the *z*-velocity dispersion value at $R = 8.5$ arcsec (Table 4) a low weight.

The central dark mass concentration is most likely a point mass. Any configuration other than a point mass must have a central density of $\rho(0) \geq 3.7 \times 10^{12}\,M_\odot\,pc^{-3}$ and a core radius of

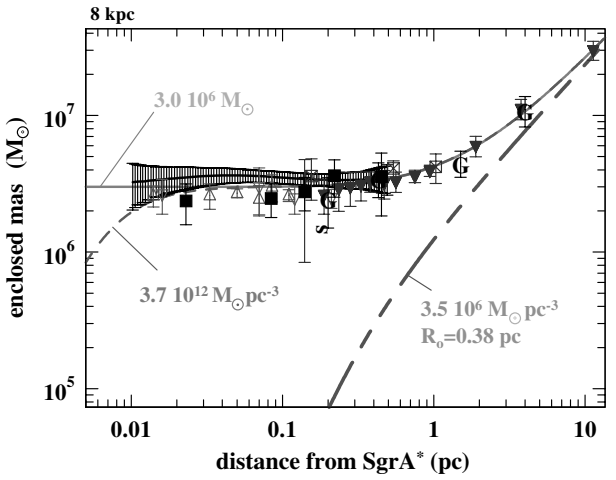

Figure 17. Mass distribution in the central 10 pc of the Galaxy obtained from stellar and gas dynamics (for $R_\odot = 8.0$ kpc). The different data points (all with $\pm 1\sigma$ uncertainties) are as follows. Bold 'G' denotes mass estimates from the ionized and neutral gas dynamics (Serabyn & Lacy 1985; Güsten et al. 1987; Lacy et al. 1991; Herbst et al. 1993; Roberts & Goss 1993). Rectangles with crosses and down-pointing triangles denote the isotropic mass modelling of Genzel et al. (1996, 1997), including Jeans modelling of stellar radial velocities (early- and late-type stars, filled down-pointing triangles) and Bahcall–Tremaine estimators of the NTT proper motions until 1996 (open down-pointing triangles). Open rectangles (with crosses) are Bahcall–Tremaine estimators of the line-of-sight-velocity data only. Open up-pointing triangles are the Bahcall–Tremaine estimators of the 1995–1996 proper motion data of Ghez et al. (1998). The new anisotropy-independent mass estimates from the present work are given as filled black rectangles (Leonard–Merritt estimators of the proper motions in (Tables 1 and 2) and as large black crosses connected by a continuous curve (Jeans model, Table 5). For comparison several model curves are shown. The long–long–short dashed curve (green in the colour version of the figure reproduced in *Synergy*) represents the mass model for the (visible) stellar cluster [$M/L(2\,\mu\mathrm{m}) = 2$, $r_{\mathrm{core}} = 0.38$ pc, $\rho(r=0) = 3.5\times10^6\,\mathrm{M_\odot\,pc^{-3}}$]. The continuous curve (light blue in the colour version of the figure reproduced in *Synergy*) is the sum of this stellar cluster, plus a point mass of $3.0\times10^6\,\mathrm{M_\odot}$. The short dashed curve (red in the colour version of the figure reproduced in *Synergy*) is the sum of the visible stellar cluster, plus an $\alpha = 5$ Plummer model, $\rho(r) = \rho(0)[1+(r/r_0)^2]^{-\alpha/2}$, of a dark cluster of central density $3.7\times10^{12}\,\mathrm{M_\odot\,pc^{-3}}$ and $r_0 = 0.0058$ pc.

$r_0 \leq 5.8$ milliparsec. For this estimate we have adopted a Plummer model with a density profile that decreases as r^{-5} outside of the core radius. In a configuration with a point mass and the visible stellar cluster [$\rho_*(0) = 3.5\times10^6\,\mathrm{M_\odot\,pc^{-3}}$, $\alpha = 1.8, r_0 = 0.17$pc] as the two main components of the mass distribution any additional mass within $\approx$0.2–0.5 pc of SgrA* must be less than $\approx1\times10^6\,\mathrm{M_\odot}$, or 32 per cent of the point mass. If one takes the LM mass distribution instead (Table 2), that limit would be between 1.1 and $2.2\times10^6\,\mathrm{M_\odot}$. Backer (1996) has shown that the proper motion of SgrA* itself is $\leq16\,\mathrm{km\,s^{-1}}$, or 50 to 100 times smaller than the fast-moving stars in its vicinity. Thus the mass enclosed within the radio size of SgrA* ($r \leq 1$ au) is $\geq10^3$ or $\geq10^5\,\mathrm{M_\odot}$, depending on whether the radio source is in momentum or energy equilibrium with the fast-moving stars (Genzel et al. 1997; Reid et al. 1999). Even the more conservative of these two limits implies a central density in excess of $10^{18}\,\mathrm{M_\odot\,pc^{-3}}$.

Our results confirm and strengthen recent work on the central mass distribution (cf. Eckart & Genzel 1996, 1997; Genzel et al. 1997, Eckart & Genzel 1997; Ghez et al. 1998). From these papers and from Maoz (1998) it appears that the most likely configuration of the central mass concentration is a massive, but currently inactive, black hole. With the parameters given above any dark cluster of stellar remnants (neutron stars, stellar black holes), low-luminosity stars (e.g., white dwarfs) or substellar objects would have a lifetime less than $\approx10^7$ yr. This is much smaller than the ages of most of the stars in the Galactic Centre, requiring that we happen to observe the Galactic Centre in a highly improbable, special period. In addition, the very steep outer density distribution of such a dark cluster implied by the mass distribution in Fig. 17 ($\rho \approx r^{-\alpha}$ with $\alpha \geq 5$) is inconsistent with any known observed dynamical system. It is also inconsistent with the results of physical models, including those of core-collapsed clusters (see the discussion by Genzel et al. 1997). Maoz points out that the only possible – albeit highly implausible – alternatives to a central black hole are a concentration of heavy bosons and a compact cluster of light ($\leq0.005\,\mathrm{M_\odot}$) 'mini' black holes.

ACKNOWLEDGMENTS

We thank David Merritt for making us aware of the mass estimators first laid out in his paper with Peter Leonard in 1989, as well as for comments on the present manuscript. We also appreciate the willingness of the ESO Director General and his staff to let us bring the SHARP camera to the NTT in 1997 and 1998. We thank Niranjan Thatte, Alfred Krabbe, Harald Kroker and the entire MPE-3D team for their help with the 3D observations on the ESO-MPG 2.2-m telescope, and for developing the new data reduction tools necessary to analyse the data set presented here. We are also grateful to the NTT team, and especially to U.Weidenmann and H. Gemperlein, for their interest and technical support of SHARP at the NTT. CP thanks E. Thiébaut for many valuable discussions. We thank Lowell Tacconi-Garman and Linda Tacconi for comments on and help with the manuscript. We are grateful to the referee for his valuable and helpful comments. Funding from the Swiss NF is gratefully acknowledged.

REFERENCES

Allen D. A., Hyland A. R., Hillier D. J., 1990, MNRAS, 244, 706
Backer D. C., 1996, in Blitz T., Teuben P., eds, Proc. IAU Symp. 169, Unsolved Problems of the Milky Way. Kluwer, Dordrecht, p. 193
Bahcall J. N., Tremaine S. C., 1981, ApJ, 244, 805 (BT)
Blum R. D., Sellgren K., DePoy D. L., 1995a, ApJ, 440, L17
Blum R. D., DePoy D. L., Sellgren K., 1995b, ApJ, 441, 603
Blum R. D., Sellgren K., DePoy D. L., 1996, AJ, 112
Bower G. C., Backer D. C., 1998, ApJ, 496, L97
Christou J. C., 1991, Experimental Astron., 2, 27
Eckart A., Genzel R., 1996, Nat, 383, 415
Eckart A., Genzel R., 1997, MNRAS, 284, 576
Eckart A., Genzel R., Krabbe A., Hofmann R., van der Werf P. P., Drapatz S., 1992, Nat, 355, 526
Eckart A., Genzel R., Hofmann R., Sams B. J., Tacconi-Garman L. E., 1993, ApJ, 407, L77
Eckart A., Genzel R., Hofmann R., Sams B. J., Tacconi-Garman L. E., Cruzalebes P., 1994, in Genzel R., Harris A. I., eds, The Nuclei of Normal Galaxies. NATO ASI Kluwer, Dordrecht, p. 305
Eckart A., Genzel R., Hofmann R., Sams B. J., Tacconi-Garman L. E., 1995, ApJ, 445, L26
Eckart A., Ott T., Genzel R., 1999, A&A, 352, L22

Genzel R., Thatte N., Krabbe A., Kroker H., Tacconi-Garman L. E., 1996, ApJ, 472, 153
Genzel R., Eckart A., Ott T., Eisenhauer F., 1997, MNRAS, 291, 219
Gerhard O. E., 1991, MNRAS, 250, 812
Ghez A., Klein B., Morris M., Becklin E., 1998, ApJ, 509, 678
Greenhill L. J., Jiang D. R., Moran J. M., Reid M. J., Lo K. Y., Claussen M. J., 1995, ApJ, 440, 619
Güsten R., Genzel R., Wright M. C. H., Jaffe D. T., Stutzki J., Harris A. I., 1987, ApJ, 318, 124
Haller J. W., Rieke M. J., Rieke G. H., Tamblyn P., Close L., Melia F., 1996, ApJ, 456, 194
Herbst T. M., Beckwith S. V. W., Forrest W. J., Pipher J. L., 1993, AJ, 105, 956
Hofmann R., Blietz M., Duhoux P., Eckart A., Krabbe A., Rotaciuc V., 1993, in Ulrich M. H., ed., Progress in Telescope and Instrumentation Technologies. ESO Report 42, 617
Kormendy J., Richstone D., 1995, ARA&A, 33, 581
Krabbe A., Genzel R., Drapatz S., Rotaciuc V., 1991, ApJ, 382, L19
Krabbe A. et al., 1995, ApJ, 447, L95
Lacy J. H., Achtermann J. M., Serabyn E., 1991, ApJ, 380, L71
Leonard P. J. T., Merritt D., 1989, ApJ, 339, 195
Libonate S., Pipher J. L., Forrest W. J., Ashby M. L. N., 1995, ApJ, 439, 202
Lindqvist M., Habing H., Winnberg A., 1992, A&A, 259, 118
Lo K. Y., Shen Z.-Q., Zhao J.-H., Ho P. T. P., 1998, ApJ, 508, L61
Magorrian J. et al., 1998, AJ, 115, 2285
Maoz E., 1998, ApJ, 494, L131
McGinn M. T., Sellgren K., Becklin E. E., Hall D. N. B., 1989, ApJ, 338, 824
Menten K. M., Eckart A., Reid M. J., Genzel R., 1997, ApJ, 475, L111
Meynet G., Maeder A., Scahller G., Schaerer D., Charbonnel C., 1994, A&AS, 103, 97
Myoshi M., Moran J. M., Hernstein J., Greenhill L., Nakai N., Diamond P., Inoue M., 1995, Nat, 373, 127
Najarro F., Hillier D. J., Kudritzki R. P., Krabbe A., Lutz D., Genzel R., Drapatz S., Geballe T. R., 1994, A&A, 285, 573
Najarro F., Krabbe A., Genzel R., Lutz D., Kudritzki R. P., Hillier D. J., 1997, A&A, 325, 700
Ott T., Eckart A., Genzel R., 1999, ApJ, 523, 248
Paczynski B., Stanek K. Z., 1998, ApJ, 494, L219
Reid M., 1993, ARA&A, 31, 345
Reid M. J., Readhead A. C. S., Vermeulen R. C., Treuhaft R. N., 1999, ApJ, 524, 816
Richstone D. et al., 1998, Nat, 395, 14
Roberts D. A., Goss W. M., 1993, ApJS, 86, 133
Schmitt J., 1995, Diploma thesis, Ludwig-Maximilian University, Munich
Sellgren K., McGinn M. T., Becklin E. E., Hall D. N. B., 1990, ApJ, 359, 112
Serabyn E., Lacy J. H., 1985, ApJ, 293, 445
Tamblyn P., Rieke G. H., Hanson M. M., Close L. M., McCarthy D. W., Rieke M. J., 1996, ApJ, 456, 206
Thatte N., Weitzel L., Cameron M., Tacconi-Garman L. E., Krabbe A., Genzel R., 1995, in Holst C. C., ed., SPIE Conference Proceedings, 2224, 279
van der Hulst J. M., Terlouw J. P., Begeman K., Zwitser W., Roeelfsema P. R., 1992, in Worall D. M., Biemesderfer C., Barnes J., eds, ASP Conf. Ser. Vol., Astronomical Data Analysis Software and Systems I. Astron. Soc. Pac., San Francisco, p. 131
Weitzel L., Krabbe A., Kroker H., Thatte N., Tacconi-Garman L. E., Cameron M., Genzel R., 1996, A&AS, 119, 531

This paper has been typeset from a TEX/LATEX file prepared by the author.